Numerical modelling of heat transfer and evaporation characteristics of cryogenic liquid propellant

Arun Tamilarasan

A thesis
submitted in partial fulfillment of the
requirements for the degree of

Master of Science in Mechanical Engineering

University of Washington

2015

Committee:

James Hermanson

John Kramlich

Alberto Aliseda

Program Authorized to Offer Degree:
Mechanical Engineering

University of Washington

Abstract

Numerical modelling of heat transfer and evaporation characteristics of cryogenic liquid propellant

Arun Tamilarasan

Chair of the Supervisory Committee:
Professor James Hermanson
Department of Aeronautics and Astronautics

Passive and active technologies have been used to control propellant boil-off, but the current state of understanding of cryogenic evaporation and condensation in microgravity is insufficient for designing large cryogenic depots critical to the long-term space exploration missions. One of the key factors limiting the ability to design such systems is the uncertainty in the accommodation coefficients (evaporation and condensation), which are inputs for kinetic modeling of phase change.

A novel, combined experimental and computational approach is being used to determine the accommodation coefficients for liquid hydrogen. The experimental effort utilizes the Neutron Imaging Facility located at the National Institute of Standards and Technology (NIST) in Gaithersburg, Maryland to image evaporation and condensation of propellants inside of metallic containers. CFD tools are utilized to infer the temperature distribution in the system and determine the appropriate thermal boundary conditions for the numerical solution of the evaporating and condensing liquid to be used in a kinetic phase change model. Using all three methods, there is the possibility of extracting the accommodation coefficients from the experimental observations.

TABLE OF CONTENTS

LIST OF FIGURES

ACKNOWLEDGMENTS

This thesis would not have been possible without the support and guidance of two individuals who assisted with the preparation and completion of this study.

First and foremost, I would like to thank my advisor, Dr. James Hermanson, for giving me the opportunity and providing excellent guidance during the course of this study. His suggestions greatly helped in determining the most useful method for conducting this study. The assistance of Dr. Jeffrey Allen of Michigan Technological University with the computational modelling is greatly appreciated. His patience with explaining and figuring out the right boundary conditions in spite of long distance communication challenges deserves a special mention. I would also like to thank the rest of the MTU team, Dr. C.K. Choi, Dr. Ezequiel Medici, Kishan Bellur, Manan Kulushreshta, Vinaykumar Konduru, Daanish Tyrewala, and Michael Kostick for their help and efforts to obtain the experimental data despite many a sleepless nights at the NIST center.

I would also like to express my gratitude for my family for their constant support and encouragement. A special mention to Avaneesh, Prakash, Rohith, Bharat, Brad, Gustavo and Luke for the many memories during grad school.

Lastly, this work would not have been possible with the support of the Early Stage Innovations Grant from NASA's Space Technology Research Grants Program (Grant #NNX14AB05G).

Chapter 1
INTRODUCTION

In recent years, space exploration has achieved new feats thanks to advancements in aerodynamics, propulsion and fuel storage techniques [18, 28]. Long duration storage of cryogenic fluids is an essential requirement for a variety of applications such as propulsion, power, and thermal management for deep-space missions. Future missions, including but not limited to manned missions to Mars, deep space exploratory missions, orbit transfer vehicles etc. [18, 34] require storage of cryogenic propellants for 5-10 years. Numerous studies, both analytical and experimental, have been conducted to meet propellant storage requirements for such missions [26, 27, 1]. One of the main problems with the long term storage of cryogenic fluids is the fluid boil-off, which occurs due to a variety of mechanisms such as self pressurization in storage containers, heat leaks, sloshing, flashing, and thermal stratification. Passive and active thermal and fluid control systems are routinely used to manipulate cryogenic liquids to mitigate boil off [8]. However, the current state of understanding cryogenic evaporation and condensation is limited, especially in microgravity conditions. This study facilitates the determination of the accommodation coefficients for cryogenic evaporation and condensation, which are key inputs to modelling the phase change phenomenon, and hence enhance the ability to design effective storage systems for cryogenic fluids. This is accomplished through a combined experimental and computational analysis. Phase-change experiments were conducted in the BT-2 neutron imaging facility at the National Institute of Standards and Technology (NIST) by introducing vapor H_2 in 10 mm Al6061 test cells placed inside a 70mm cryostat while the computational thermal model was developed using ANSYS Fluent.

1.1 Motivation for research

Evaporation and condensation coefficients, often referred to as accommodation coefficients, are derived from kinetic theory and represent the fraction of molecules striking the liquid surface that undergo phase change [2]. The accommodation coefficient is considered to be a thermodynamic property of kinetic models of evaporation and condensation. Accurate prediction of the rate of phase change typically requires a measured value of the accommodation coefficient. Unfortunately, there is significant discrepancy in the reported values of the accommodation coefficient.The value of the accommodation coefficient depends on the surface nature such as the presence of impurities, type of material, and the state of the fluid such as a sudden change in temperature or pressure in the interface. For water alone the values of the accommodation coefficients have varied by two to three orders of magnitude depending on the researcher or the method used to determine this coefficient. An indication of why there is such a large discrepancy in the mass accommodation coefficient can be inferred from the experiment described by Cammenga et al [6]. and reiterated in Marek and Straub [23] . An evaporation coefficient of 0.002 was found for water in a glass vessel, but when the glass vessel was replaced with a copper vessel the evaporation coefficients increased two orders of magnitude to values between 0.25 and 0.38. With the exception of the vessel wall material, both experiments were conducted in the same apparatus. Thus, the reported values of the accommodation coefficient do not necessarily reflect the local conditions nor the non-uniform evaporation that occurs due to the presence of a contact line. The thermal model developed in this study feeds liquid and solid temperature profiles near the evaporating region of the system under observation into a transition film model. This micro-scale then estimates the accommodation coefficients based on a modified form of the Schrage Equation. A detailed write-up of the transition film model can be found in Appendix 1 for further reading and reference. The transition film model is developed from the ground up by Michigan Technological university.

1.2 Research Objectives

A new type of experiment with complementary computational analysis has been undertaken to determine the evaporation and condensation coefficients for liquid hydrogen. A combined modelling and experimental effort is being pursued with the experiments conducted at the Neutron Imaging Facility (NIF) located at the National Institute of Standards and Technology (NIST) located in Gaithersburg, Maryland. The focus of this thesis is the computational model developed in Fluent and validating the model to reproduce the experimental conditions.

The design of the experiment is such that no temperature measurements can be made on the inside of the test cell and thus no transient heat transfer data is available for the cryostat. In order to extract the evaporation and condensation coefficients from the transition film model, a thermal boundary condition on the interior wall of the test cell is required. The temperature profile that will be obtained from the numerical simulations will be used as inputs for this transition film model.

The numerical study for the evaporation of liquid hydrogen is done in three stages:

- Dry test simulations to characterize the thermal response of the test cell.
- Evaporation simulation with a solid block resembling the bulk liquid meniscus's shape and thermal properties similar to those of the liquid to determine the thermal boundary conditions near the meniscus.
- Evaporation simulation with mass transfer based on the Hertz-Knudsen-Schrage equation to visually comprehend the evaporation behaviour of liquid hydrogen.

In short, the main objective of this study is to characterize the thermal response of the test cell from the dry test simulations. This enables the extraction of interior wall temperature profile of the test cell from the line sink simulations with confidence. In addition, the thermal model also attempts to understand information not easily accessible from experiments such

as the convective behaviour of the coolant gas in the cryostat and temperature distribution along the length of the cryostat.

Chapter 2

NUMERICAL SIMULATION METHOD AND SET-UP

The numerical study has been conducted using the commercial CFD code ANSYS Fluent, which has been used for a variety of engineering applications [12, 11, 26]. This commercial finite volume package along with Design Modeller and ANSYS Meshing is used for geometry creation and meshing respectively. The methodology adopted to perform the numerical study can be summarised in Figure 2.1. The ANSYS Fluent model is a 2-D axisymmetric model of the experimental set-up. Although a 3-D model would more closely reproduce the experimental conditions, the 2-D axisymmetric model is an appropriate choice given the computational time and resources needed. The assumption of axisymmetry implies that there are no circumferential gradients in the flow, but that there may be non-zero circumferential velocities [9]. *Superior*,a high performance computing cluster at Michigan technological university was used in obtaining results presented in this study .

2.1 Governing Equations

The dry test simulation and the line sink simulations are single-phase flows with heat transfer. The evaporation simulation with mass transfer is a multiphase flow that uses the Volume of Fluid method to keep track of the evaporating interface. All the three simulations use the energy and flow equations inbuilt in the solver. A brief overview of the governing equations that are solved in Fluent to arrive at the solution is described in this chapter.

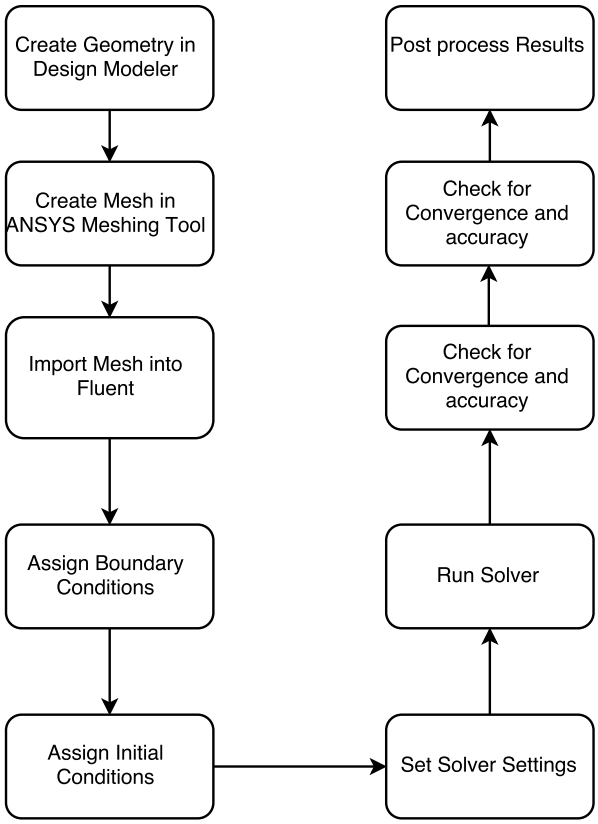

Figure 2.1: Flowchart summarising the numerical methodology

2.1.1 The Energy Equation

ANSYS Fluent solves the energy equation in the following form:

$$\frac{\partial}{\partial t}(\rho E) + \nabla \cdot (\vec{v}(\rho E + p)) = \nabla \cdot (k_{eff} \nabla T - \sum_j h_j \vec{J}_j + (\bar{\bar{\tau}} \cdot \vec{v})) \tag{2.1}$$

where k_{eff} is the effective conductivity (k+k_t, where k_t is the turbulent thermal conductivity, defined according to the turbulence model being used), and $\vec{J}$ is the diffusion flux of species j . The first three terms on the right-hand side of the equation represent energy transfer due to conduction, species diffusion, and viscous dissipation, respectively. The term, E is given by:

$$E = h - \frac{P}{\rho} + \frac{v^2}{2} \tag{2.2}$$

where the sensible enthalpy, h is defined as:

$$h = \sum_j Y_j h_j + \frac{P}{\rho} \tag{2.3}$$

where Y_j is the mass fraction of the species j.

2.1.2 The Mass Conservation Equation

For 2-D axisymmetric geometries, the continuity equation is given by:

$$\frac{\partial \rho}{\partial t} + \frac{\partial}{\partial x}(\rho v_x) + \frac{\partial}{\partial r}(\rho v_r) + \frac{\rho v_r}{r} = S_m \tag{2.4}$$

where x is the axial coordinate, r is the radial coordinate, v_x is the axial velocity and V_r is the radial velocity.S_m is the mass added to the continuous phase from the dispersed second phase (e.g., due to vaporization of liquid droplets) and any other user-defined sources. For a closed system such as the dry test and the line sink simulations, S_m is zero.

2.1.3 Momentum Conservation Equations

The axial and radial momentum conservation equations for a 2-D axisymmetric geometry are given by:

$$\frac{\partial}{\partial t}(\rho v_x) + \frac{1}{r}\frac{\partial}{\partial x}(r\rho v_x v_x) + \frac{1}{r}\frac{\partial}{\partial r}(r\rho v_r v_x) = -\frac{\partial p}{\partial x} + \frac{1}{r}\frac{\partial}{\partial x}\left[r\mu\left(2\frac{\partial v_x}{\partial x} - \frac{2}{3}(\nabla\cdot\vec{v})\right)\right] + \frac{1}{r}\frac{\partial}{\partial r}\left[r\mu\left(\frac{\partial v_x}{\partial r} + \frac{\partial v_r}{\partial x}\right)\right] + F_x \tag{2.5}$$

and

$$\frac{\partial}{\partial t}(\rho v_r) + \frac{1}{r}\frac{\partial}{\partial x}(r\rho v_x v_x) + \frac{1}{r}\frac{\partial}{\partial r}(r\rho v_r v_r) = -\frac{\partial p}{\partial r} + \frac{1}{r}\frac{\partial}{\partial r}\left[r\mu\left(2\frac{\partial v_r}{\partial r} - \frac{2}{3}(\nabla\cdot\vec{v})\right)\right] + \frac{1}{r}\frac{\partial}{\partial r}\left[r\mu\left(\frac{\partial v_r}{\partial r} + \frac{\partial v_x}{\partial r}\right)\right] + F_r + \frac{2}{3}\frac{\mu}{r}(\nabla\cdot\vec{v}) - 2\mu\frac{v_r}{r^2} \tag{2.6}$$

where F_x is the force component in the axial direction and F_r is the force component in the radial direction.

2.2 Geometry and Meshing

The Fluent thermal model for the dry test and line sink model includes the test cell, the lid, the sample stick upto the first radiation baffle, the cryostat copper block, which serves as the heat input to the system, and the sample well enclosure. This enclosure is an aluminum canister secured to the copper block. The line sink model, in addition to the above zones, has a fluid and a solid zone, with thermal properties similar to that of the cryogenic liquid modelled inside the test cell.The domain along with the above mentioned components used in the dry test simulations and line sink simulations can be seen in Figures 2.2 and 2.3.

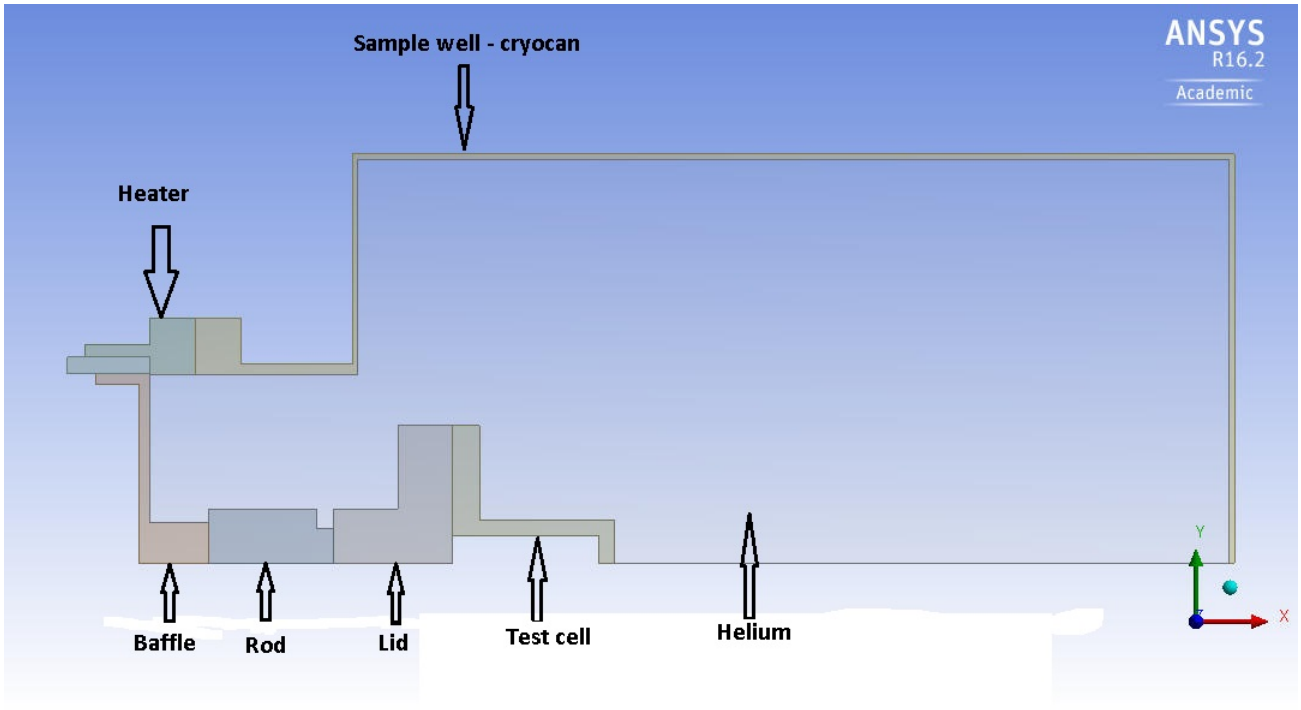

Figure 2.2: Domain for the Dry test Simulation

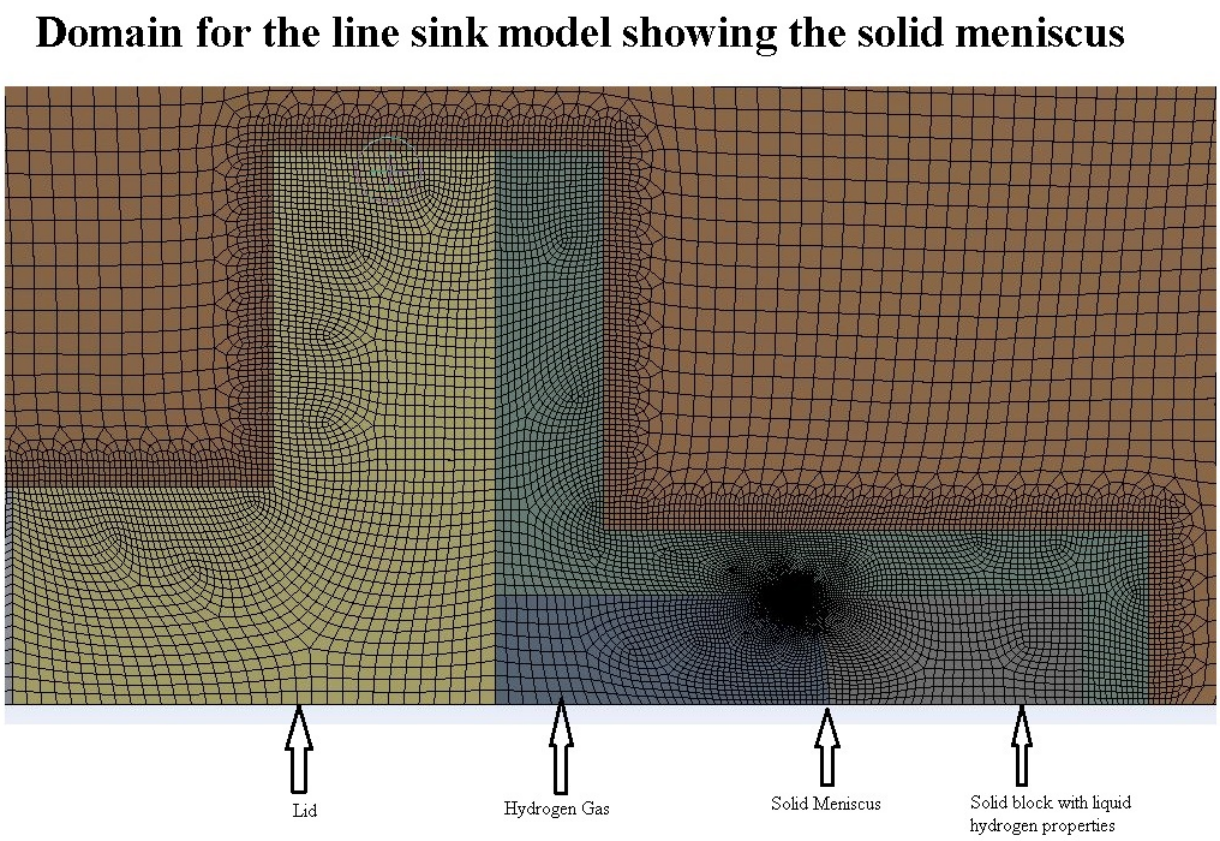

Figure 2.3: Domain for the Line Sink Simulation

2.3 Boundary and Initial Conditions

The boundary and initial conditions for the dry test and the line sink model are similar with a few extra conditions imposed for the line sink model to simulate the effect of evaporation.

A transient temperature profile consisting of the experimental heater temperature was assigned as a temperature boundary condition to the walls of the copper block. The rest of the walls in the model were assumed to be adiabatic. Heat is transferred to and from the test cell by a combination of: a) conduction through the radiation baffle and sample stick, and b) convection through the helium space surrounding the test cell and contained within the sample well enclosure. The walls facing the helium region have a no-slip boundary condition.

The amount of helium in the sample well could not be precisely measured and the amount of helium changes when the test cell is changed. The pressure in the sample well was estimated to be between 10 Pa and 200 Pa through analytical calculations. The pressure of the helium gas was assigned in the numerical model such that best agreement occurs between the experimental and numerical data. The initial conditions for the model were defined by the initial temperature and pressure of the gas in the cryostat. The initial temperature and pressure used in the dry-test simulation is given below:

$$P = 185 \text{ Pa}$$
$$T = 20 \text{ K}$$

For the line sink simulations, to simulate the effect of the evaporating liquid, a heat flux was applied for a length of $10\mu m$ along the solid meniscus. The equation for determining the value of heat flux,$\dot{q}$ is given by:

$$\dot{q} = \dot{m} * h_{fg} \tag{2.7}$$

where $\dot{m}$ is the mass flow rate and is derived from experimental values of volume flow rate multiplied by the density of liquid hydrogen, and h_fg is the latent heat of evaporation in kJ/kg.

The initial conditions for this model were influenced by the thermal conditions existing in

the previous time step. As no information was available on the thermal gradient that exists across the domain, a steady state simulation was run prior to the transient simulations. The copper block remained at a constant 23 K during both the transient and steady state simulations. The gaseous hydrogen and the solid block with the liquid hydrogen properties were assigned an initial temperature of 21 K, which was the saturation temperature at which the experiment was carried out. The gaseous hydrogen inside the test cell was set to a pressure of 120,00 Pa or 1.2 bar while the helium surrounding the test cell was at 185 Pa.

The material properties used for the solid and fluid materials in the domain were temperature-dependent and obtained from the NIST cryogenic materials database [22]. Material properties were included as piecewise linear data with respect to temperature in the thermal model. Plots of thermal diffusivity of Copper, Aluminum 6061 and Stainless Steel 316 used in the simulations are shown in Figures 2.4, 2.5 and 2.6. Inclusion of the temperature dependent material properties was crucial to the accuracy of the thermal model developed in Fluent.

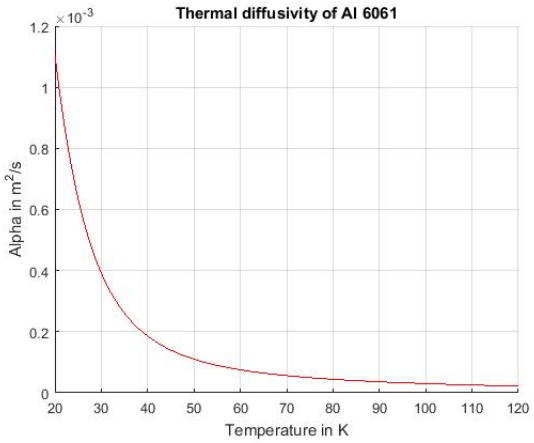

Figure 2.4: Thermal Diffusivity of Aluminum 6061

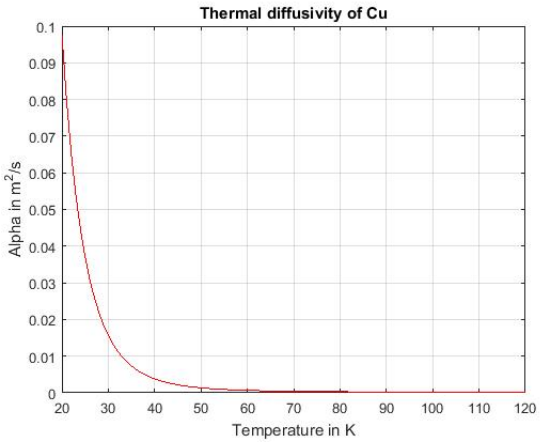

Figure 2.5: Thermal Diffusivity of Copper

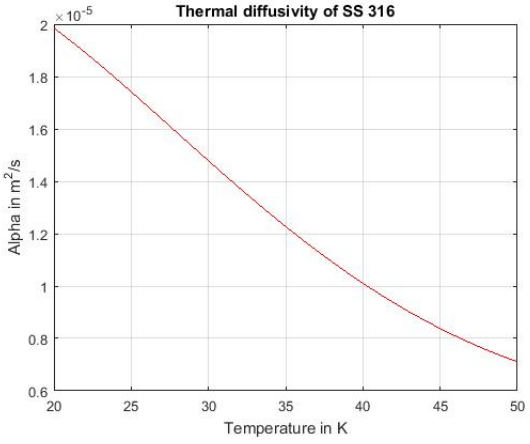

Figure 2.6: Thermal Diffusivity of SS 316

2.4 Solver Settings

The Energy equation and the k-ϵ equation were incorporated in the above-described models to perform the thermodynamic and flow analysis and solve for the temperature and velocity distribution in the domain. The Rayleigh number for the Helium in the sample well was estimated to be around $2 * 10^3$, which implies a laminar flow in the helium region. In the Rayleigh number calculations, the thermal expansion coefficient for helium equals to 1/T, where T is the absolute temperature. Although the flow regime in the Helium space is laminar, the enhanced wall treatment option in the k-ϵ model yielded better results with a higher time step value than that of the laminar model. A comparison of results with both the laminar and the $k - \epsilon$ model is attached in the appendix for reference. The SIMPLEC (Semi-Implicit Method for Pressure Linked Equations-Consistent) was used for the pressure-velocity coupling. The SIMPLEC algorithm converges 1.2-1.3 times faster than SIMPLE while the computational cost per iteration remains the same [9]. A least square cell based gradient interpolation method is used since it is recommended for regular meshes, as it is accurate and minimizes false diffusion in natural convection problems[36].The Body-force-weighted scheme was used for pressure interpolations as it works well with buoyancy driven flows where the body forces in the momentum equations are known a priori [9]. This scheme computes the face pressure by assuming that the normal gradient of the difference between pressure and body forces is constant. The Second Order Upwind scheme is used for the discretization of momentum equations. For density and energy spatial discretization, the Third Order MUSCL scheme was used, which improves spatial accuracy for all types of meshes by reducing numerical diffusion [33]. For all other turbulence spatial discretization, a Second Order Upwind scheme was used.

The time step in the simulations performed was determined by the Courant number which determines the propagation speed of information on the mesh. The Courant number is defined as:

$$C_o = \frac{u\Delta t}{\Delta x} \tag{2.8}$$

where Δt is the time step, Δx is the smallest mesh element length, and u is the flow velocity through the small element. In this study, a time step size of 0.1 was considered for both the models to keep the courant number below 0.25.

2.5 Evaporation Simulations with mass transfer

The evaporation model in Fluent uses the Volume of Fluid (VOF) method to keep track of the evaporating interface. The VOF method was first developed to solve free boundary problems by Hirt and Nichols in 1981 [14]. The VOF method is a surface tracking technique applied to a fixed Eulerian mesh [31]. This method assumes that the fluids in play are immiscible. In each control volume, the volume fraction of all phases sum to unity. The fields for all variables and properties are shared by the phases and represent volume-averaged values,as long as the volume fraction of each of the phases is known at each location.Thus the variables and properties in any given cell are either purely representative of one of the phases, or representative of a mixture of phases, depending on the volume fraction values. For instance, if the q^{th} fluid's volume fraction is denoted as α_q, then the following conditions are possible:

- $\alpha_q = 0$: The cell is empty
- $\alpha_q = 1$: The cell is full
- $0 < \alpha_q < 1$: The cell contains the interface between the q^{th} fluid and one or more other fluids.

Since the model comprised of two different phases, there was a jump in properties with a change in the phase. In numerical simulations, this jump needs to be modelled carefully over the interface which is spread over a few grid cells. The variation of properties with a two phase model are described below:

$$\rho = \alpha_v \rho_v + \alpha_l \rho_l \tag{2.9}$$

$$\mu = \alpha_v \mu_v + \alpha_l + \mu_l \tag{2.10}$$

$$C_p = \alpha_v C_{pv} + \alpha_l + C_{pl} \tag{2.11}$$

$$k = \frac{k_v k_l}{k_v \alpha_l + k_l \alpha_v} \tag{2.12}$$

The interface location, at any instant, is tracked from the gradient of the volume fraction of the phases.This was accomplished using an User Defined Function that is loaded onto the model. Mass transfer happens only at the interface and is zero at all other locations in the fluid.

The contributions made by Hertz and Knudsen to use the kinetic theory of gases have been vital to understand the evaporation and condensation phenomena [13]. The rate of evaporation and condensation can be described through the Kinetic Theory of gases [19]. According to kinetic theory, the rate of evaporation depends on the liquid pressure and temperature. Similarly the rate of condensation depends on vapor pressure and temperature. They proposed that the evaporation from the liquid surface of the Knudsen layer takes place according to a half range Maxwellian distribution. The Hertz-Knudsen equation can be stated as:

$$\dot{m} = \sqrt{\frac{M}{2\pi R_u}} \left[C_c \left(\frac{P_v}{\sqrt{T_v}} \right) - C_e \left(\frac{p_{sat}(T_l)}{\sqrt{T_l}} \right) \right] \tag{2.13}$$

where v stands for the vapor phase and l for the liquid phase. The accommodation coefficient for evaporation (C_e) represents the fraction of liquid molecules which get converted to vapor upon striking the liquid-vapor interface. Similarly, the accommodation coefficient for condensation (C_c) refers to the fraction of vapor molecules which get condensed upon striking the liquid-vapor interface. On the other hand, this relation proposed had a shortcoming that it did not account for the flow velocity which results due to the phase change on either side of the interface.

In Fluent, the liquid-vapor mass transfer is governed by the following vapor transport equation and is based on the equation proposed by Lee [21]:

$$\frac{\partial}{\partial t}(\alpha_v \rho_v) + \nabla \cdot (\alpha_v \rho_v \vec{V_v}) = \dot{m_{lv}} - \dot{m_{vl}} \tag{2.14}$$

where $\dot{m}_{lv}$ and $\dot{m}_{vl}$ denote the rates of mass transfer due to evaporation and condensation respectively in $kg/s - m^3$. Evaporation, by default, is defined as positive mass transfer. Hence, based on temperature regime existing at the interface,

- If $T_l > T_{sat}$ (evaporation): $\dot{m}_{lv}$ = coeff * Volume fraction of liquid * Density of liquid $* \frac{(T_l - T_{sat})}{T_{sat}}$

- If $T_v < T_{sat}$ (condensation): $\dot{m}_{vl}$ = coeff * Volume fraction of vapor * Density of vapor $* \frac{(T_{sat} - T_v)}{T_{sat}}$

The value of coeff was tuned accordingly to match the desired evaporation and condensation rates. More information on the evaporation-condensation model used in Fluent can be found in Fluent Theory Guide. The UDF used in the model is attached in the Appendix. Also, this model has been verified against the 1-D Stefan problem, the results of which can be found in [35].

2.5.1 Boundary and Initial Conditions

The evaporation model includes the inner walls of the test cell and the evaporating fluid zone. The wall temperature boundary conditions on the outer walls of the test cell were obtained from the line sink model. The remaining walls in the domain were assigned an adiabatic wall boundary condition. Hydrogen vapour was assigned as the primary fluid and hydrogen liquid was set to be the secondary fluid. This arrangement, as dictated by Fluent, helped with smoother convergence. The vapour and liquid were assumed to be at equilibrium and at saturation. Once the solution was initialized, the liquid was patched onto the domain using the Adapt $\rightarrow$ Region option in Fluent. The initial conditions for this model depends on the thermal conditions existing in the previous time step of the experimental data.

2.5.2 Solver Settings

The Volume of Fluid method with an implicit formulation was chosen as the multiphase technique for the evaporation simulation. The implicit method was chosen as the preferred solver type to have the modified High Resolution Interface Capturing (HRIC) scheme for the spatial discretization of volume fraction equations, which sets the interface description to sharp [24]. For the VOF multiphase model, upwind schemes are generally unsuitable for interface tracking because of their numerical diffusive nature [9]. Also the central differencing schemes, while generally able to maintain the sharpness of the interface, are boundless and usually give unphysical results. In order to avoid these problems, a modified version of the High Resolution Interface Capturing (HRIC) scheme was used. The modified HRIC scheme consists of a non-linear mix of upwind and downwind differencing. The modified HRIC scheme provides improved accuracy for VOF calculations when compared to QUICK and second-order schemes and is less computationally costly than the Geo-Reconstruct scheme. The implicit body force formulation is included to account for the effects of surface tension forces, which tends to diminish the contributions of convective and viscous terms. Segregated algorithms converge poorly unless partial equilibrium of pressure gradient and body forces is taken into account [32].

For pressure velocity coupling, the PISO scheme is used. This scheme is of the same family as the SIMPLE algorithm. However, PISO improves on the momentum balance after the pressure correction is applied by utilizing two additional corrections: neighbour correction and skewness correction. This requires more computational time per iteration but it reduces the total number of iterations needed to achieve convergence, particularly with transient properties [3, 17] . The body force weighted scheme was chosen for pressure interpolations. The THIRD Order MUSCL scheme was utilised for the spatial discretization of momentum and energy equations while the Second Order Upwind scheme was used for the density equations. An User Defined Function that is based on the Lee model was added to the model to specify the interfacial mass transfer conditions.

Chapter 3

EXPERIMENTAL SET-UP OVERVIEW

Experiments examining the bulk evaporation and condensation of liquid hydrogen were conducted during January 2015 at the NIST (National Institute for Standards and Technology) Center for Neutron Research (NCNR) in the Neutron Imaging Facility. Although the focus of this thesis is the computational part of the research, a brief overview of the experimental set-up is given below. The design and the successful trials of the evaporation experiments were largely due to the efforts of the Michigan Tech team.

A schematic of the cryostat is shown in Figure 3.1. The sample well is a 70-mm diameter Aluminum canister that passes through concentric vacuum and cryogenic annuli and then extends below these annuli into an evacuated chamber through which the neutron beam passes. The outer most cryogen annulus is filled with liquid nitrogen that evaporates and vents to the atmosphere thereby maintaining a temperature of 77 K.An inner liquid helium jacket also evaporates that helps to maintain the sample well temperature at about 4 K provided no external heating occurs. The rate of helium evaporation and therefore the rate of cooling and minimum temperature is controlled through a throttling valve that can be adjusted. For additional cooling a vacuum can be pulled on the vapor side of the throttling valve. The helium throttle valve is part of an assembly referred to as the copper block that is positioned at the separation between the cryostat and the lower chamber through which the neutron beam passes. An electric heater is also located in this copper block. The stainless tube with radiation baffles to which the test cell is attached is referred to as the sample stick. At the bottom of the sample stick is the test cell connected through a stainless steel 316 L lid and where evaporation or condensation occurs. The test cell is made of aluminum with a wall thickness of 3 mm and an internal diameter of 5 mm. The lid includes a vapor passage

that can be seen in Figure 3.1 (e). The temperature of the copper block can be set and controlled. Thermal energy is transferred to and from the test cell by a combination of (i) conduction from the copper block through an aluminum radiation baffle and down a stainless tube to the test cell, and (ii) convection in low pressure helium gas circulating between the test cell and the sample well housing. Thermal neutrons (energy 25 meV) neutrons from a fission reactor penetrate the cryostat. The large neutron scattering cross section of hydrogen as compared to that of aluminum allowed for signal-to-noise levels sufficient for imaging the location of the liquid hydrogen surface [16].The scintillator used for imaging is a 7.6 mg/cm^2 Gadoxysulfide screen with a thickness of 20 m. An Andor NEO sCMOS (scientific Complementary Metal Oxide Semiconductor) camera with a pixel pitch of 6.5 m and variable exposure time is used to capture the images. An 85 mm Nikon lens with a PK13 extension tube is used to image the scintilator light. This detector configuration had sufficient spatial ($<$50 m) and temporal ($<$10 s) resolution to measure local curvature and evaporation rates of liquid hydrogen. Additional details on the Neutron Imaging Facility (NIF) and the hydrogen infrastructure used for the experiments described herein can be found in Hussey et al [16, 15]. Instrumentation for these experiments consisted of pressure measurements on the test cell feed line and manifold as well as temperature measurements on the test cell exterior. Three Lakeshore silicon diode DT-670 temperature sensors were mounted on the outside of the test cell and secured in place by the use of custom fabricated 306 stainless steel springs that were wrapped around the test cell exterior. A fourth sensor was suspended in the sample well near the test cell to measure the temperature of the circulating helium gas. Test cell temperatures were logged using a Lakeshore model 340. The uncertainty in the test cell measurements is $\pm$ 0.25 K. The uncertainty in the sensor placed in the copper block (NTC RTD X45720 sensor) to log the heater temperature is $\pm$ 0.1 K. The temperature of the copper block sensor and the sample holder temperature sensor were logged using a Lakeshore Model 331 that was also used to control the heater temperature. Pressures were logged using two mensor pressure transducers. One sensor (mensor CPG 2500) was connected to the hydrogen gas feed connected to the test cell. The second pressure transducer (Mensor DPG 15000) was

connected to the manifold. The uncertainty in the pressure measurements is 0.01 %.

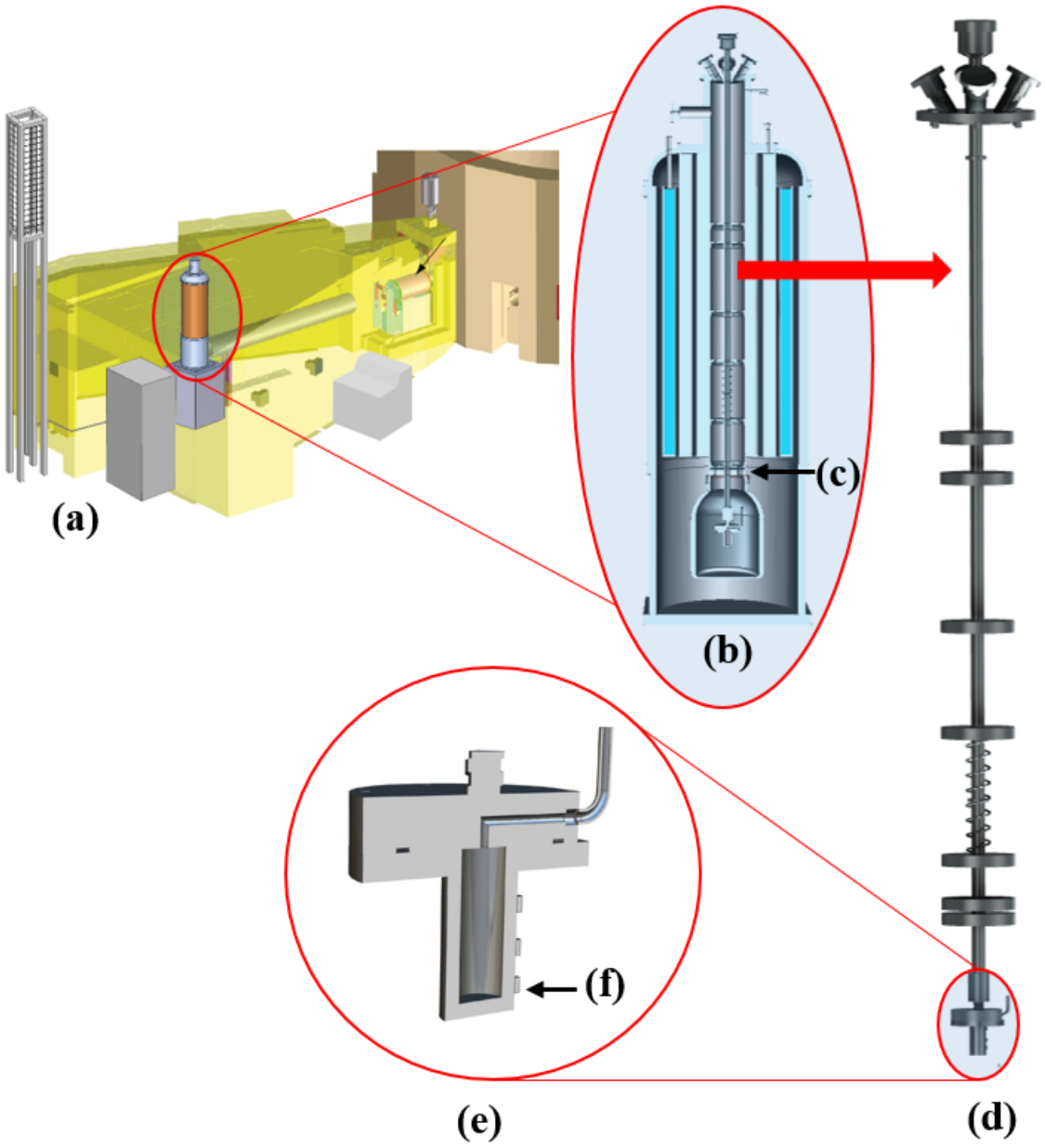

Figure 3.1: Overview of experiments conducted at the NIST Neutron Imaging Facility(NIF). (a) Neutron Imaging Facility with cryostat in beam line. (b) Cryostat with testcell installed. (c) Location of copper block used for heating and cooling the test cell and helium gas in the sample well. (d) Sample holder with 10-mm test cellattached. (e) Cutaway view of the 10 mm diameter test cell and lid. (f) sensors located on test cell. Image is a courtesy of [5]

Chapter 4

RESULTS AND DISCUSSION

4.1 Dry Test Simulations

In this section, the results obtained by simulating the dry tests for the 10 mm Aluminum test cell are presented. Temperatures were measured at four different points in the domain and the results were compared against the experimental values to validate the model. The sensor locations in the the domain is shown in Figure 4.1.

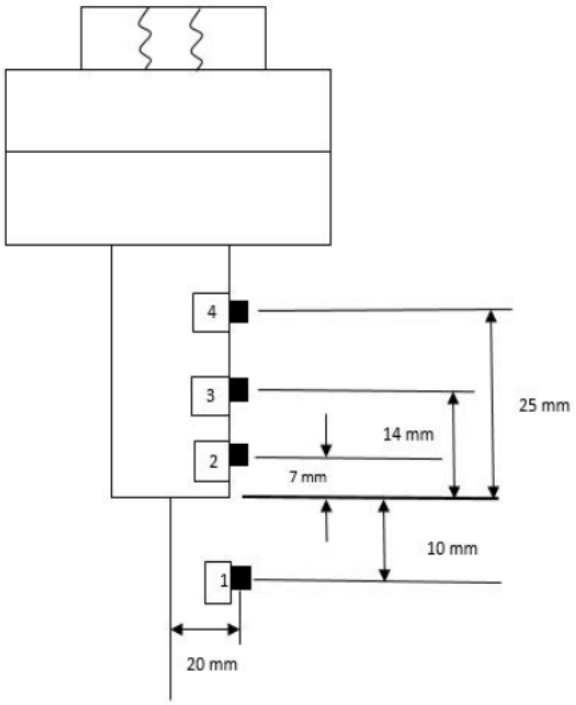

Figure 4.1: Sensor locations on the test cell

The dry test experiments are experiments conducted with no fluid present inside the test cell

to establish the overall heat transfer characteristics associated with tests where liquid was present.The numerical model exhibits good agreement with the experimental measurements. A plot of transient temperature profile for both the experimental and numerical curves for the sensors 2 and 3 can be seen in Figures 4.2 and 4.3.A non-dimensionalised plot of the same can be seen in Figures 4.4 and 4.5. This plot helps to visually compare the numerical time scale against that of the experiment.

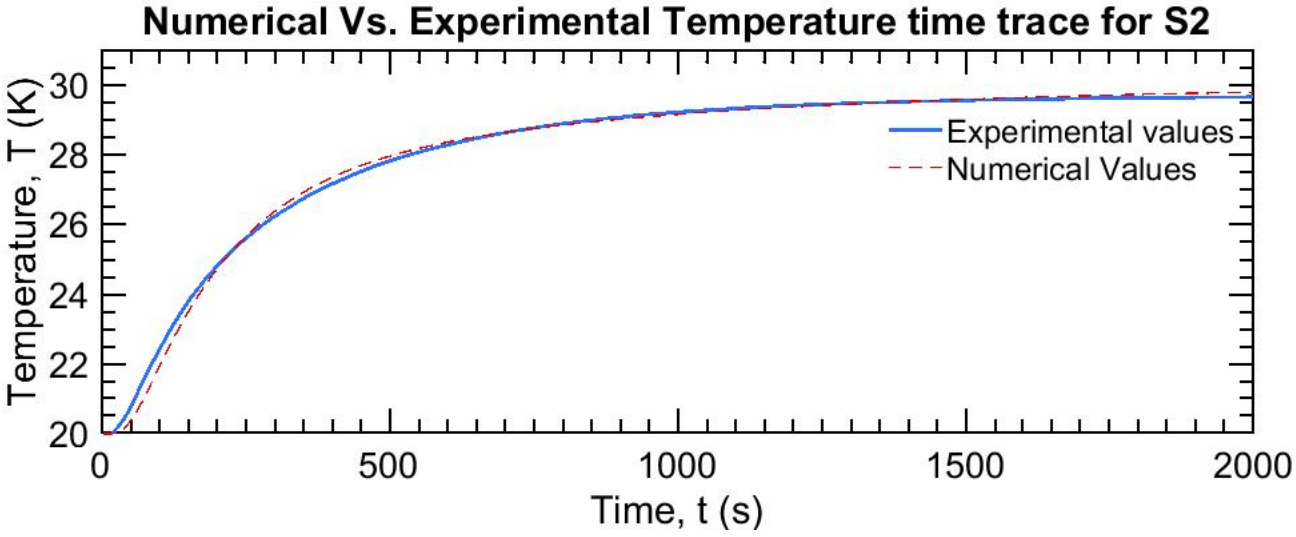

Figure 4.2: Experimental and Numerical time response for the dry test cell experiment with the 10-mm diameter Aluminum test cell for Sensor 2

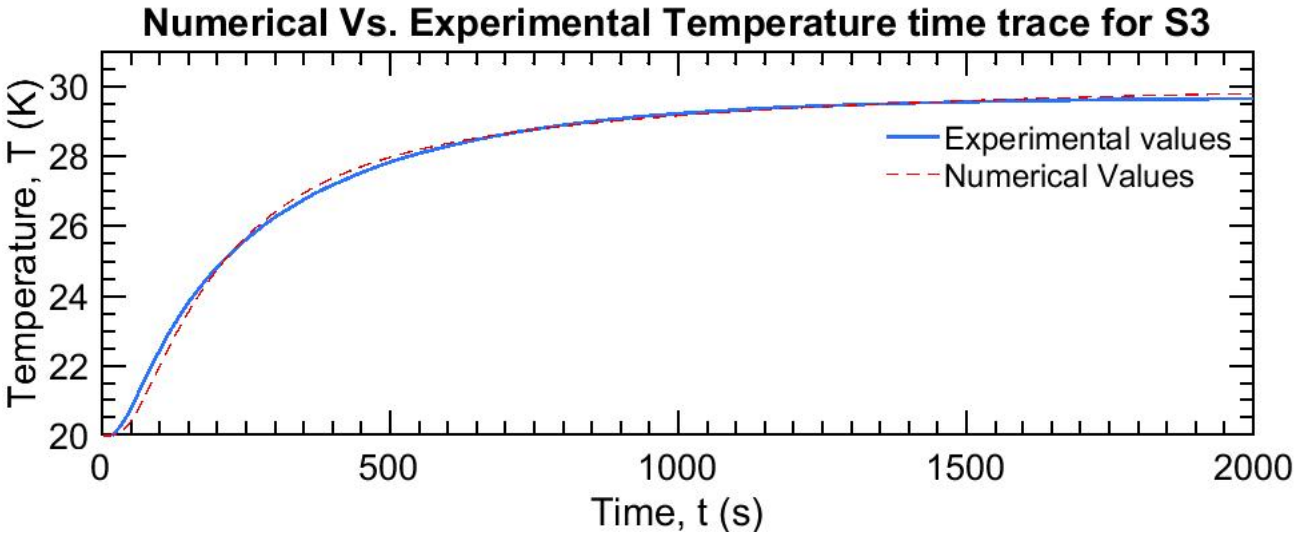

Figure 4.3: Experimental and Numerical time response for the dry test cell experiment with the 10-mm diameter Aluminum test cell for sensor 3

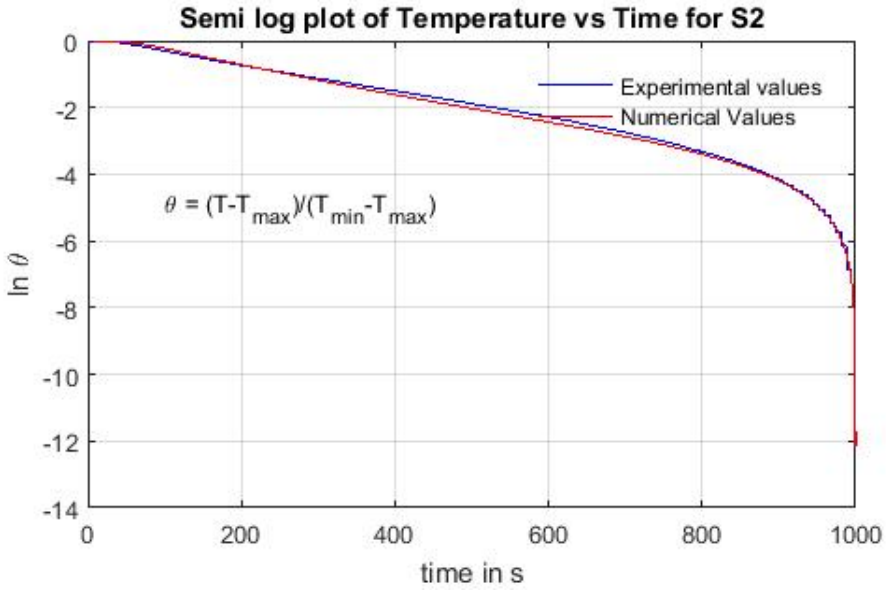

Figure 4.4: Semi log plot of Experimental and Numerical time response for the dry test cell experiment with the 10-mm diameter Aluminum test cell for Sensor 2

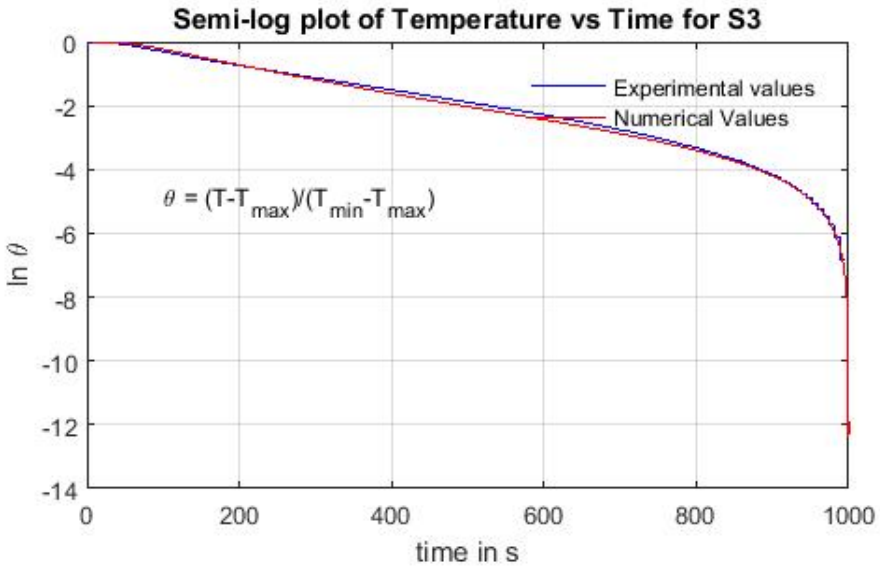

Figure 4.5: Semi log plot of Experimental and Numerical time response for the dry test cell experiment with the 10-mm diameter Aluminum test cell for Sensor 3

The precise dimensions of the sample well were not known. For instance, the thickness of the outer aluminum wall of the sample well could not be accurately measured. The thermal model was tuned to account for the actual thermal mass present in the system. The numerical temperature profiles for all the sensors on the test cell were well matched with the experimental data. The objective of the dry test simulations was to characterise the transient thermal response of the test cell and serve as a base model on which the evaporation model can be built. Although the heat input to the test cell is a combination of conduction and convection, the numerical values of heat flux at the wall boundaries show that the dominant mode of heat transfer into the test cell is via conduction. Figure 4.6 shows the values of heat fluxes at the convective and conductive boundaries in the domain. To account for the transient heat flux at the boundaries, the entire domain needed to be modelled instead of restricting the focus to the test cell where evaporation occurs. This would significantly increase computational time and resources.

Heat Flux in W/m^2			
	Name of Boundary	Time = 1000 seconds	Time = 2000 seconds
Conductive Boundaries	Baffle- Rod wall	83	19.7
	Rod-Lid wall	100	23.75
	Lid- Test cell wall	-5.7	-1.34
Convective Boundaries	Baffle walls	-0.105	-0.03
	Rod walls	0.75	0.18
	Lid walls	0.019	0.0018
	Test cell walls	1.55	0.47

Figure 4.6: Heat Flux at convective and conductive boundaries in the domain

4.1.1 Temperature and Velocity Distribution

At the start of the simulation, the entire domain was assumed to be at 20 K and there was no stratified temperature distribution. However, the initial sensor readings from the experiment show otherwise. As the solution progressed with time and the test cell gets heated, thermal stratification occurred throughout the domain which in turn gives rise to a buoyancy driven flow in the helium space. The solution progressed long enough that the absence of an initial temperature distribution does not significantly affect the accuracy. The thermal model provides information on the convective behaviour of the coolant gas that is not accessible from experimental data. Figures 4.7 and 4.8 show the temperature and velocity contour plots in the domain at 2000 seconds. The thermal stratification in the domain, as seen in Figure 4.7, suggests that conduction is the primary mode of heat transfer since most of the heat is accumulated near the top of the system. The magnitude of velocity in the helium region is very low, which is in agreement with a laminar flow as demonstrated by the low Rayleigh number. It should also be noted that the recirculation regions near the sample well wall and the test cell are opposite in flow direction since the helium is colder than the solid components.

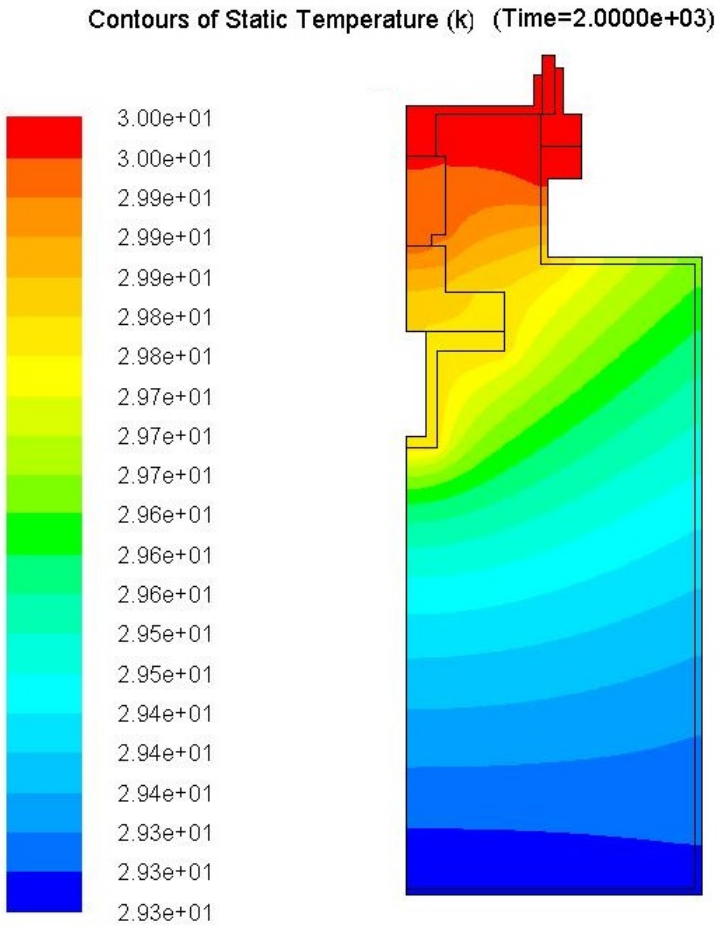

Figure 4.7: Contour plot of temperature for the 10-mm Al Dry test simulations

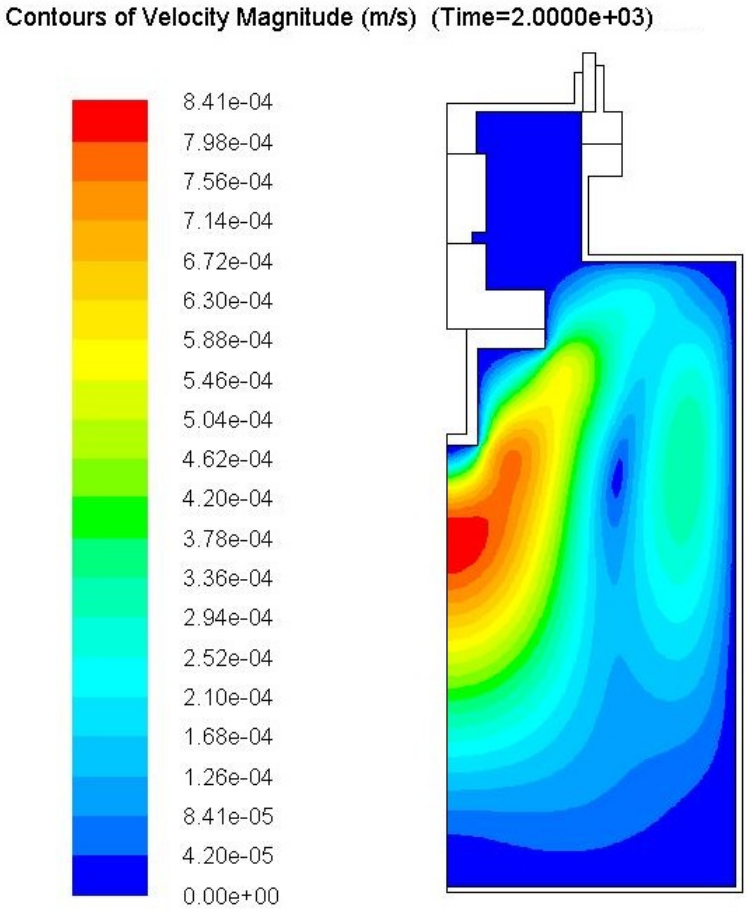

Figure 4.8: Contour plot of velocity for the 10-mm Al Dry test simulations

4.2 Line Sink Simulations

With the thermal response of the test cell characterised from the dry test simulations and finding that the major mode of heat transfer in and out of the test cell is by conduction, it was evident that the entire domain, from the heater to the test cell, needed to be modelled in order to accurately capture the thermal conditions. In addition to being computationally intensive, the inlet and exhaust hydrogen ports are not effectively captured, because the rotational symmetry assumption does not hold as can be seen in Figure 3.1 e. As a method to estimate the thermal boundary conditions that exists near the gas-liquid interface and on the walls of the test cell, a solid block with thermal-diffusive properties similar to that of the liquid hydrogen at the corresponding saturation temperature was modelled inside the test cell. This model did not account for any mass transfer effects, but the effect of evaporation was simulated through the line sink. The boundary conditions obtained was used as inputs in the evaporation simulations based on the Schrage equations (Eq. 2.13) as well as in the transition film model being developed by Michigan Tech. A segment of the experimental data where the meniscus remained relatively stable was chosen as the input for this simulation. The Rayleigh number of the liquid inside the test cell was estimated to be of the order of $1e^3$, which is less than the critical Rayleigh number for convection cells to appear. The advantage of this model was that the meniscus shape can be accurately modelled while taking advantage of the fact there is minimum convection happening in the liquid. A time lapse image of the liquid in the test cell can be seen in Figure 4.9, which shows a stable meniscus with respect to shape throughout the condensation and evaporation regimes.

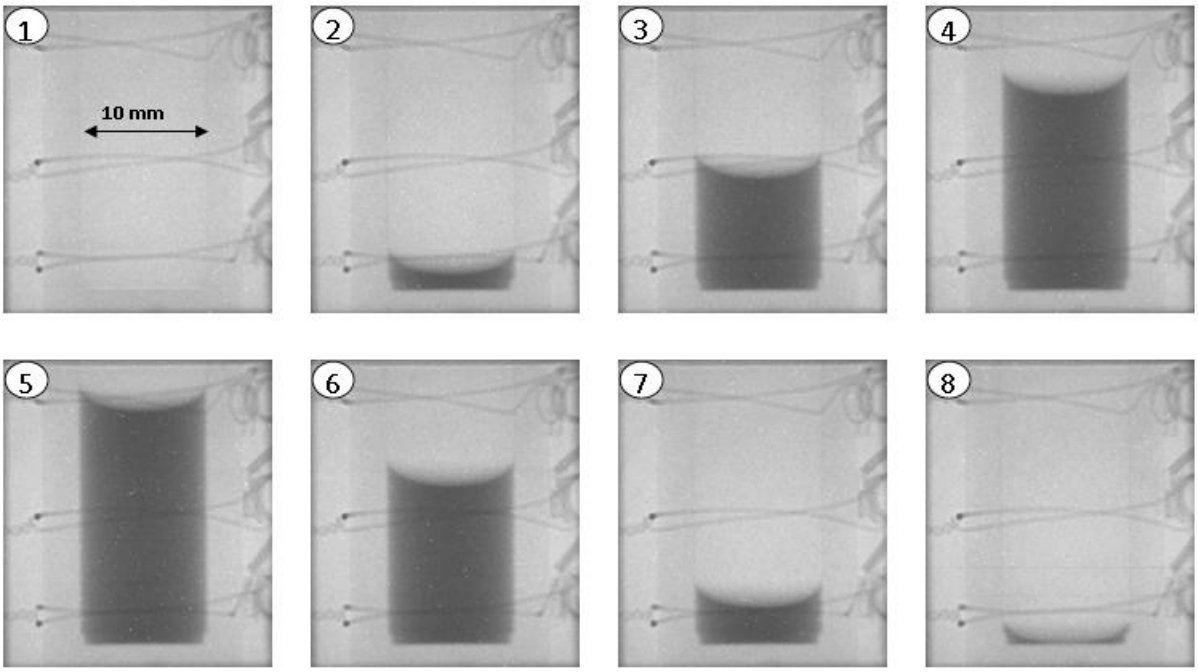

Figure 4.9: Time Lapse Image of the liquid meniscus, courtesy of Kishan Bellur

In the above figure, tiles 1 through 4 show the condensation of liquid hydrogen inside the 10-mm diameter Aluminum test cell while the remaining tiles show the evaporation of the liquid. Images were obtained at a 10 second interval which helped estimate the condensation/evaporation rates.

The plots of experimental sensor temperature with time, as seen in Figure 4.10 show

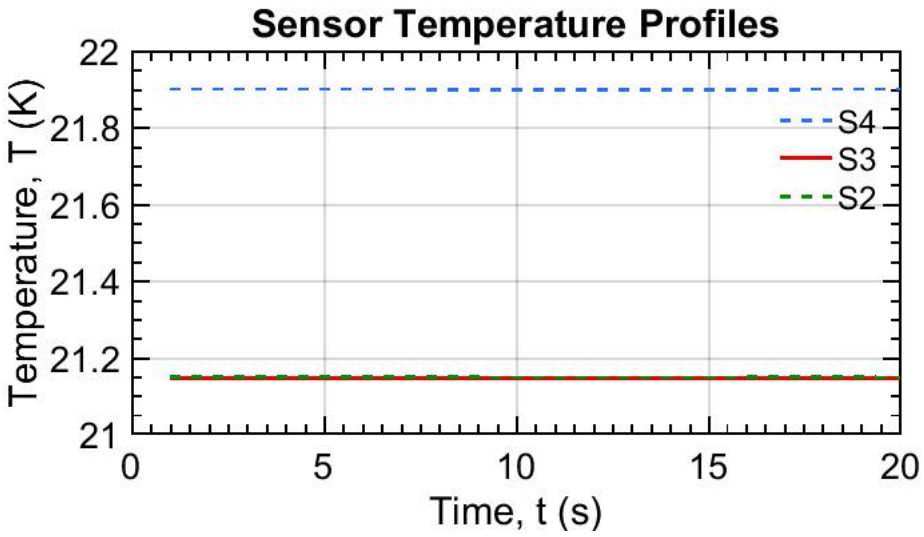

Figure 4.10: Experimental Sensor temperature profiles

that the system can be assumed to be at steady state during this particular period. The line sink simulation was, hence, run as a steady state simulation.The corresponding temperature profile on the inner wall of the test cell, obtained from the numerical modelling, is shown in Figure 4.11. The temperature profiles on the outer walls of the test cell are illustrated in Figures 4.12 and 4.13. Once the thermal characteristics have been reasonably matched with the experimental data, the temperature boundary conditions along the walls of the test cell were exported to the evaporation model. The line sink model primarily assisted with the transition from the dry test model to the evaporation model.

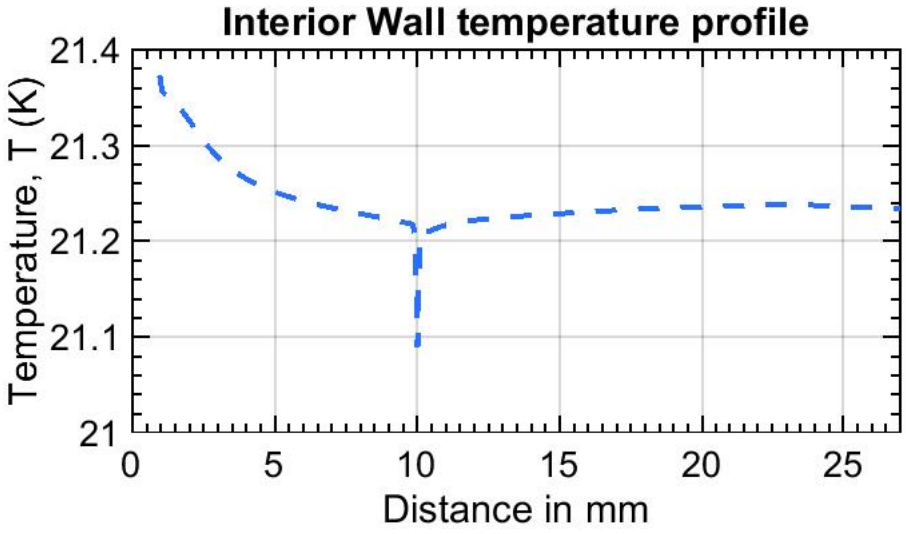

Figure 4.11: Interior Wall temperature profile of the test cell with simulated effect of evaporation

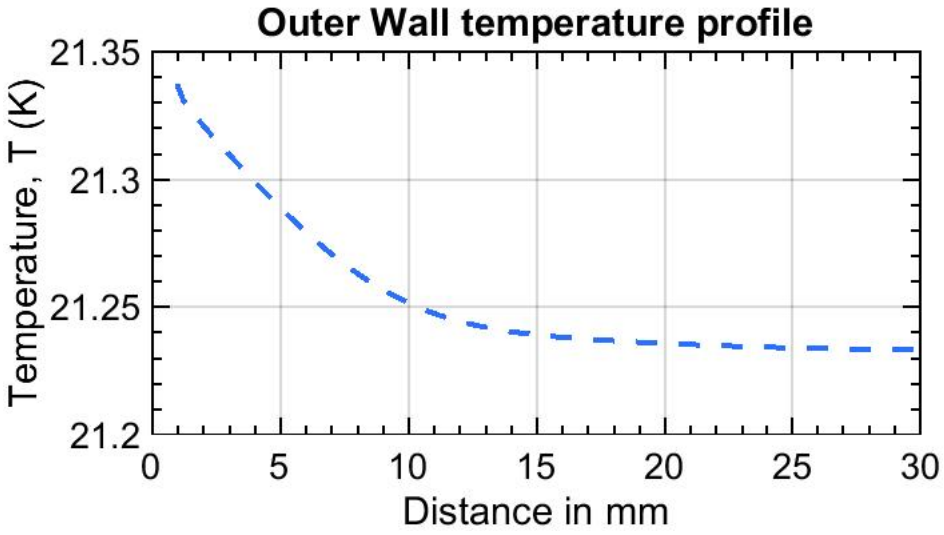

Figure 4.12: Exterior vertical wall temperature profile of the test cell with simulated effect of evaporation

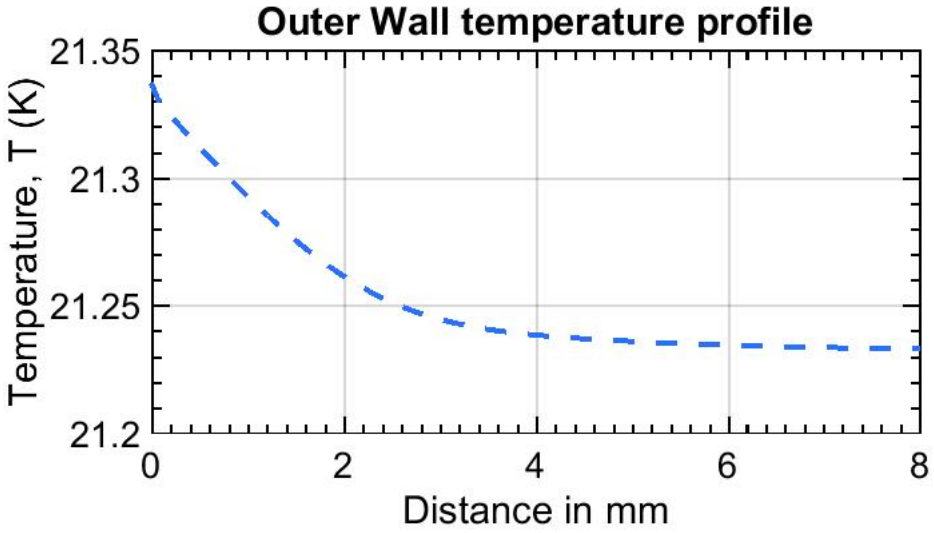

Figure 4.13: Exterior horizontal wall temperature profile of the test cell with simulated effect of evaporation

The temperature dip in Figure 4.11 was because of the heat flux applied on the meniscus to simulate the effect of evaporation. The heat flux was applied over a very small length of 10 μm since 60-90 % of the evaporation was expected to occur in the contact line region [29]. However, this temperature jump did not translate to the outer wall of the test cell.

4.3 Evaporation simulations with mass transfer

A numerical model incorporating evaporation was developed to give some insight into the heat transfer and mass flux that occurs at the fluid-vapor interface. This model is generic in nature and is not intended to exactly reproduce the actual conditions in the experiment. One of the main reasons for this being that the Schrage equation can only be used for flat interfaces. The accommodation coefficients for the evaporation of liquid hydrogen are calculated using the transition film model, which is a micro-scale model focusing solely on the events happening in the vicinity of the meniscus. The Fluent evaporation model also did not account for surface tension or the contact angle. A short description of the transition film model and how the temperature boundary conditions from Fluent were used can be found in the appendix. The phase distribution in the test cell at time, $t = 0$ can be seen Figure 4.14.

Evaporation occurs only at the interface with maximum evaporation rate near the walls as seen in Figure 4.15. The average experimental volume flow rate was of the order of $1e^{-9}$ mm^3/s and it would take around 2000 seconds for the fluid to completely evaporate from the test cell. The multiphase flow equations demand higher computation resources to be solved. In addition, the grid resolution needed to capture the evaporation phenomenon that occurs near the interface was high. The computational time and resources demanded by Fluent for the evaporation simulation was high enough that the simulation was run for a total time of only 200 seconds to infer the evolution of the temperature profile as well as the velocity profile in the domain. The liquid-vapour interface remained relatively stable during the simulated time. The evolution of the temperature profiles can be seen in Figures 4.16, 4.17 and 4.18 which are the temperature contours of the fluid domain at time 9, 30 and 200

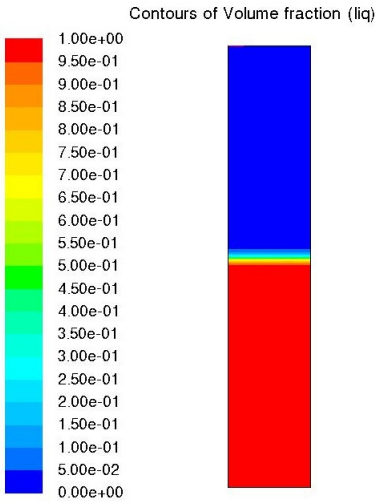

Figure 4.14: Contour plot of evaporation rate

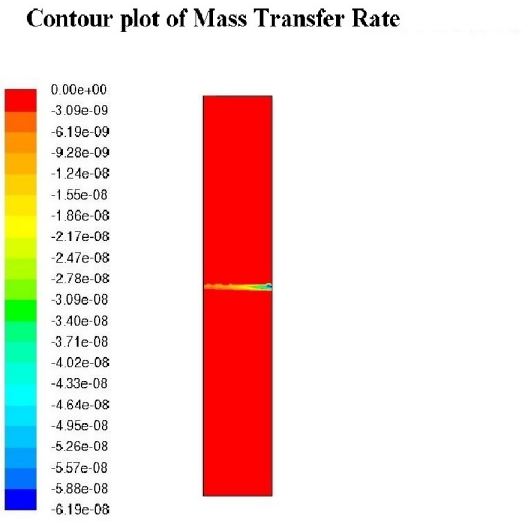

Figure 4.15: Contour plot of Volume fraction of Phases

seconds respectively. Heat was added to the test cell from the sides and the bottom, which was accounted for in the model by the temperature boundary conditions applied on the outer walls of the test cell. In addition to heat added to the liquid from the walls of the test cell, due to the relatively higher thermal diffusivity of the vapour, there was heat transfer from the vapour to the liquid as well. The velocity contour, as shown in Figure 4.19, shows that there is no convection happening in the liquid while a weak convection can be seen in the vapour domain. This observation was in accordance with the calculated Rayleigh number. In addition, the plot of heat flux, as seen in Figure 4.20 at the inner wall of the test cell showed a jump in heat flux value at the interface location. This is again attributed to the difference in thermal diffusivity between the gas and the liquid.

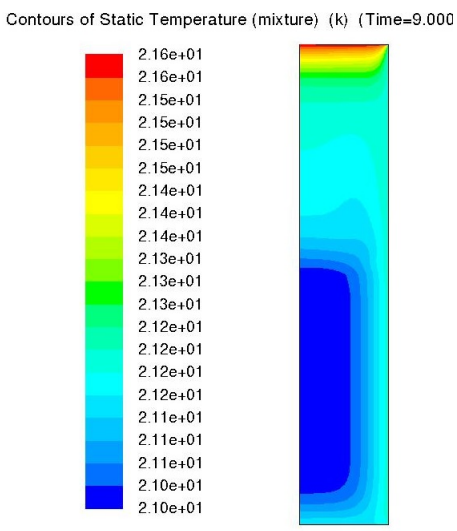

Figure 4.16: Temperature contour at 9 seconds

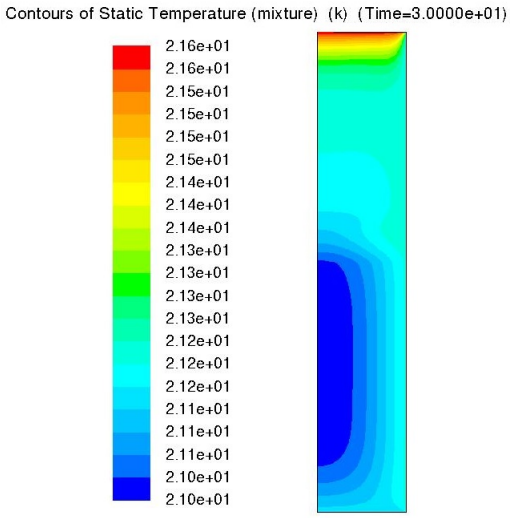

Figure 4.17: Temperature contour at 30 seconds

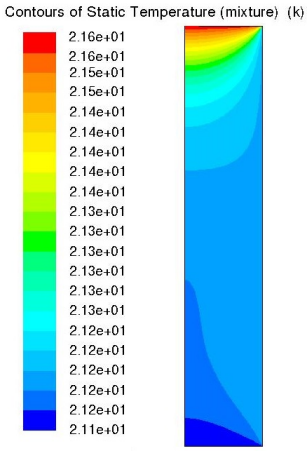

Figure 4.18: Temperature contour at 200 seconds

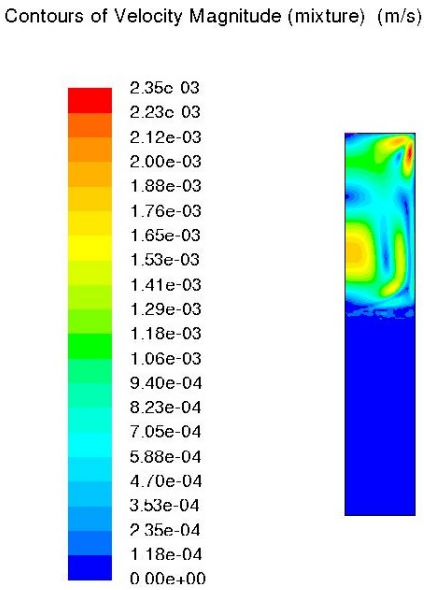

Figure 4.19: Velocity contour at 200 seconds

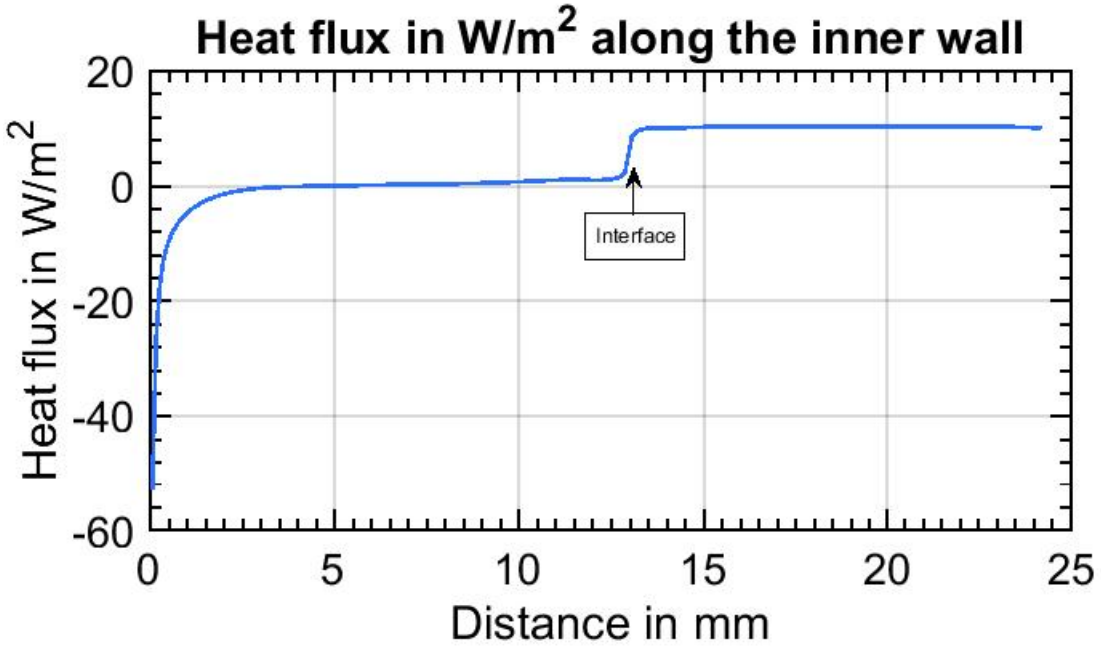

Figure 4.20: Heat flux at the inner wall of the test cell

Chapter 5

CONCLUSIONS AND FUTURE WORK

In this thesis, a computational model was successfully developed to characterize the transient thermal response of the test cell and components under cryogenic conditions. Comparison with experimental data helped validate the accuracy of the Fluent model. In order to aid in the determination of accommodation coefficients, temperature profiles on the inner walls of the test cell were successfully extracted using the line sink model. The current solver in Fluent uses the traditional Hertz-Knudsen-Schrage formulation for mass transfer which is valid only for a flat interface. The simulation revealed that the maximum rate of evaporation was at the liquid-vapour interface and near the wall. There was negligible fluid motion in the liquid while a weak convection was present in the gas, which was in accordance with the analytical Rayleigh number calculations. Open FOAM's solver has the capability to model fluid evaporation based on the modified form of the Schrage equation that can account for surface tension and curvature effects, which are essential to match the experimental results. Once the accommodation coefficients have been successfully extracted from the transition film model, an evaporation simulation using Open FOAM can help better understand the fluid behaviour during evaporation. Future work will revolve around the evaporation behaviour in microgravity conditions and using a different material for the test cell to infer the dependence of accommodation coefficients on the wall material . It is our hope that the combined experimental and modelling approach can be used to better understand the phase change phenomenon in cryogenic liquids and hence improve the effectiveness of cryogenic storage systems.

Appendices

Appendix 1

TRANSITION FILM MODEL

The Transition film model is the work of Kishan Bellur, Michigan technological University and the following section is an extract from his work. A brief description of the model and its relevance with the CFD simulation is described below.

Liquid vapour phase change is a complex, multi-scale problem and different phase change models have been used to quantify and predict mass transfer rates. These broadly fall under three categories: diffusive, kinetic or quantum mechanical. Diffusive models rely on partial vapour pressure as a trigger mechanism for evaporation. They predict the same phase change rates despite the solid wall material or the wetting characteristics and curvature of the liquid vapor interface. The evaporative mass flux is taken to be only a function of the interfacial area and the concentration difference between the liquid and the interface (which is taken to be a saturated vapour for modelling purposes). These models are typically applied to systems where surface area is huge, such as open reservoirs. When the exposed surface area is smaller and comparable to the meniscus size, such as in porous structures or capillary tubes, kinetic models have been shown to be more accurate [10]. Kinetic theory based models can account for the effect of the wall, the location and size of the meniscus, curvature, interface temperature and disjoining pressure effects [25]. The classical kinetic theory has provided the basis for understanding and modelling evaporation for over a century. Hertz [18] measured evaporation rates of mercury and from a theoretical analysis concluded that there exists a maximum rate of evaporation that depends on the temperature of the interface and the properties of the liquid. Knudsen [20] carried out similar experiments on evaporation of mercury and his results consistently indicated that the measured evaporation rate is lesser than the maximum rate suggested by kinetic theory. He introduced the concept

of an evaporation coefficient to account for the deviation from the maximum evaporation rate. The velocity distribution of the molecules is described by the Boltzmann equation A.1 .

$$\frac{\partial f}{\partial t} + c_i \frac{\partial f}{\partial x_i} = S(f) \tag{A.1}$$

where $S(f)$ denotes the collision term that describes the change of the velocity distribution due to intermolecular collisions and c_i is the velocity. In equilibrium, the velocity distribution function does not change with time and $S(f) = 0$. Hence the solution yields the famous Maxwellian distribution A.2.

$$f_m = n\left(\frac{m}{2k\pi T}\right)^{3/2} exp\left(-\frac{m}{2KT}(c_x^2 + c_y^2 + c_z^2)\right) \tag{A.2}$$

where k is the Boltzmann constant, n denotes the density number of particles, m is the molecular mass, T is temperature and c_i is the velocity.

At a distance far away from the interface the velocity distribution is Maxwellian but if the interface itself is assumed not to be a disturbing influence then the Maxwell distribution would exist even in close proximity to the interface. In equilibrium, the rate of evaporation is equal to the rate of condensation. Assuming that the distribution is Maxwellian close to the interface, the Hertz-Knudsen equation for net phase change is the difference between rates of evaporation and condensation as shown by A.3:

$$J = \frac{1}{\sqrt{2\pi mk}}\left(\sigma_e \frac{P_{sat}(T^L)}{\sqrt{T^L}} - \sigma_c \frac{P^V}{\sqrt{T^V}}\right) \tag{A.3}$$

where σ_e and σ_c are the evaporation and condensation coefficients, subscripts V and L denote the vapor and liquid phases respectively. Schrage [**?**] assumed that the distribution in the vapor is better represented by a Maxwellian but with a net drift velocity (Ub) as shown in equation A.4. He further states that the evaporation and condensation coefficients could be equal and calls it the âĂIJcondensationâĂİ coefficient.

$$f_s = n\left(\frac{m}{2k\pi T}\right)^{3/2} exp\left(-\frac{m}{2KT}((c_x - U_b)^2 + c_y^2 + c_z^2)\right) \tag{A.4}$$

Schrage proves that the effect of the drift velocity is negligible if $U_b^2 << kt$. Using SchrageâĂŹs modified distribution, equation A.5 was obtained by Barrett and Clement [4]

$$J = \frac{1}{\sqrt{2\pi mk}}\left(\frac{\sigma_e}{1-0.5\sigma_c}\frac{P_{sat}(T^L)}{\sqrt{T^L}} - \frac{\sigma_c}{1-0.5\sigma_c}\frac{P^V}{\sqrt{T^V}}\right) \tag{A.5}$$

Comparing A.5 with **??** it is seen that when $\sigma_e = \sigma_c$, SchrageâĂŹs equation predicts twice the mass flux as predicted by the Hertz-Knudsen expression. It is to be noted that all these analytical studies were performed for evaporation from a planar surface. If there exists a curvature and a contact line, the local pressure in the liquid film varies and significantly influences evaporation.

The contact line is an apparent intersection of the three phases- solid, liquid and vapor. The contact angle is the apparent angle between the liquid and solid as measured through the liquid. The contact line is described as a continuum region that terminates in an adsorbed layer. The normal stress in the bulk is mostly influenced by capillary pressure or curvature. The adsorbed film is a non-evaporating film where intermolecular forces dominate. This film is on the order of nanometers and is not optically accessible. The contact line region or the transition film region is influenced by both intermolecular forces and capillarity. It has been shown that for polar/non-wetting liquids, 60-90% of the evaporation occurs at the contact line region [29] . The amount of mass transfer through the interface depends on the size of the contact line region as well as local thermodynamic properties

A.0.1 Technique for determining accommodation coefficients

In order to solve for the evaporative mass flux using the kinetic model, the liquid phase temperature is required. The liquid temperature depends on the temperature of the solid in contact with the liquid. To obtain both the liquid and wall temperature, a conjugate heat transfer model that uses representative boundary conditions is used.The temperature profile on the inner wall of the test cell obtained from the line sink model is used.The non-uniform evaporative flux in the contact line region is obtained from the kinetic model using the results of the CFD model as thermal boundary conditions. The total evaporated mass

can then be computed by integrating the non-uniform mass flux from the adsorbed film to the bulk meniscus.

A.0.2 Transition region Kinetic model

The modified form of the Schrage equation that accounts for curvature [37] and surface tension effects [30] is given by A.6:

$$J = \frac{2\alpha}{2-\alpha}\left(\frac{m}{2\pi RT_{lv}}\right)^{1/2}\left[\frac{p_v M h_{fg}}{RT_v T_{lv}}(T_{lv}-T_v) - \frac{V_l P_v}{RT_{lv}}(\Pi+\sigma k) + \frac{Mgp_v}{RT_v}x\right] \tag{A.6}$$

where J is the evaporative heat flux, α is the accommodation coefficient, Π is the disjoining pressure(a pressure reduction due to solid-liquid interaction in a thin film), σ is the surface tension, k is the curvature while all other parameters represent standard thermodynamic properties.

The numerical model for the phase change in the transition region is built based on the formulation provided by Wee at al [38] and builds off of the code developed by Fritz. Using a lubrication approximation, the film evolution/evaporation can be expressed as a nonlinear third order ODE such that all parameters and thermal properties are expressed in terms of the film thickness A.7:

$$h_{xxx} - \frac{3h_{xx}^2 h_x}{1+h_x^2} - \frac{h_{xx}h_x}{(r_{ij}-h)^2} + \frac{h_x(1+h_x^2}{(r_{ij}-h)^2)} + \frac{\gamma}{\sigma}\left(\frac{1+h_x^2}{r_{ij}-h} + H_{xx}\right)\frac{dT}{dx} + \frac{1}{\sigma}(1+h_x^2)^{1/2}\left(\frac{dP_l}{dx} + \frac{d\Pi}{dx}\right) = 0 \tag{A.7}$$

where h is the film thickness ,r_{ij} is the radius of the cylinder, p_l is the pressure in the liquid, $\gamma = d\sigma/dt, h_x, h_{xx}, h_{xxx}$ are the first, second and third derivatives respectively.

The model is built using a one sided formulation approach. The liquid properties such as density, conductivity, etc. are more dominant in the liquid than in the vapour. The model only updates the liquid properties in each step of the simulation and assumes uniform properties in the vapour phase. Further, in the thin transition film, the bond number (gravitational forces/surface forces) is lesser than 1. Hence the effect of gravity is neglected. To keep the model in a steady state mode at each step of the simulation, the mass flux across

the interface as determined by A.6 is assumed to be replenished by liquid flow from the bulk meniscus. This conservation of mass at each step creates a pressure gradient along the simulated domain. The flow is modelled using a lubrication approximation of the Navier-Stokes equation in polar coordinates,

$$\frac{1}{r}\frac{\partial}{\partial r}\left(r\frac{\partial u}{\partial r}\right) = \frac{1}{\mu_l}\frac{dp_l}{dx} \tag{A.8}$$

where μ_l is the viscosity, u is the velocity, r is the local radius,dp_l/dx is the pressure gradient.

The equation is solved by applying a no slip boundary condition at the wall and a free surface boundary condition at the interface(balancing viscus terms with surface tension terms).

$$\text{at } r = r_{ij}\ u = o$$
$$r = r_{ij} - h\ -\mu\frac{\partial u}{\partial r} = \frac{d\sigma}{dx}$$

Upon solving A.8 using the given boundary conditions, an expression for uprq is obtained. The mass flux can then be expressed by A.9

$$J = \int_{r_{ij}-h}^{r_{ij}} \rho_l[u(r)]2\pi r dr \tag{A.9}$$

Using the result of A.6 and A.9, dp_l/dx is evaluated for use in A.7. A simplified energy balance is expressed by A.10

$$k_l\frac{\partial}{\partial r}\left(r\frac{\partial T}{\partial r}\right) = 0 \tag{A.10}$$

A constant wall temperature boundary condition along with a heat flux boundary condition is used to solve the equation. The heat flux accounts for the conduction and the energy lost due to evaporation.

$$\text{at } r = r_{ij}\ T = T_{wall}$$
$$r = r_{ij} - h\ k_l\frac{dT}{dr} = \dot{m}_{evap}h_{fg}$$

Integrating A.10 from wall to the interface (ie r_{ij} to $r_{ij} - h(x)$), the interfacial temperature is obtained A.11

$$T_{lv} = -\frac{h_{fg}}{k_l}(r_{ij} - h)ln\left(\frac{r_{ij}}{r_{ij} - h}\right) + \dot{m}_{evap} + T_{wall} \tag{A.11}$$

Curvature gives rise to a pressure jump across the interface as described by the Young Laplace equation. To effectively model the pressure balance, Wayner [37] proposed A.12.

$$p_v - p_l = \sigma k + \Pi \tag{A.12}$$

The geometry of interest has two planes of curvature, one due to the meniscus and the other due to the radius of the cylinder, in the azimuthal direction. Hence an effective 3D curvature is computed A.13.

$$k = \frac{1}{r - h}(1 + h_x^2)^{-1/2} + h_{xx}(1 + h_x^2)^{-3/2} \tag{A.13}$$

For a flat wetting surface, the disjoining pressure is modeled by A.14 considering only the intermolecular London-van ver Waals forces[7]. More sophisticated models of disjoining pressure exist such as the logarithmic model by Holm and Goplen [30] or the contact angle based model by Wu and Wong [39]. For computation simplicity and due to the lack of data available for cryogens, the polynomial model given by A.14 is used.

$$\Pi = \frac{A}{h^3} \tag{A.14}$$

where,A is the dispersion constant and $6\Pi A$ is the Hamaker constant.

The evaporation in the model is accounted for by the Hertz-Knudsen-Schrage equation that has been expanded to include the effects of surface tension and curvature (equation A.7). The evaporation/condensation coefficients are inputs to the transition film evaporation model. The curvature is modeled using the augmented Young-Laplace equation by Wayner [37].

Assuming no evaporation in the adsorbed film region, the equation A.7 is set to zero and the film thickness for this condition to be achieved is computed using a root finding algorithm considering both the 3D curvature and the disjoining pressure. This is then used as one of the initial conditions of the model. Other initial conditions include the derivatives of film thickness and the superheat condition (difference between wall and vapor temperature). Although formulated as an initial value problem, the current approach is to vary the initial conditions such that the curvature from the simulation can be matched to the curvature obtained by the Young-Laplace curvefit of the liquid vapor interface acquired from Neutron Imaging. The ODE is numerically solved using a 2^{nd} order Runge-Kutta method using a simple backward Euler finite difference scheme for local interface temperatures and surface tension gradients. At each step in the simulation, the evaporated mass flux and interfacial temperature is computed and the corresponding parameters are updated.

Using the Young-Laplace curve fits from the neutron images as physical boundary conditions, a shooting method is employed for the transition film model. The initial conditions at the adsorbed film were varied such that the slope and curvature obtained from the model at its end boundary condition matches the bulk meniscus represented by the Young-Laplace curve fit within a 1% error. Assuming no evaporation in the adsorbed film region, the nonuniform evaporative flux obtained in the transition region is then integrated along the liquid interface to obtain the total evaporation rate. The temperature gradient at the wall obtained from the CFD model serves as the thermal wall boundary condition.

The code is built using a modular approach comprising of various submodels to account for curvature, disjoining pressure and other parameters. The model contains a library of fluids (currently- water, pentane, octane, hydrogen and methane) with the parameters built in and different geometries can be implemented if necessary. The code is built such that switching between different fluids or geometries is straightforward. This enables adaptability of the code to model both hydrogen and methane evaporation in cylinders of different geometries and cell materials.

Appendix 2

MASS TRANSFER UDF

This chapter lists the User Defined Function used in Fluent to dictate the mass transfer conditions.

```
#include "udf.h"

DEFINE_MASS_TRANSFER(evap_udf,cell,thread,from_index,from_species_index,
to_index,to_species_index)
{
 real m_lg,vg;
 real T_SAT = 21; /* Saturation Temperature*/
 Thread *gas, *liq;
 liq = THREAD_SUB_THREAD(thread,to_index);
 gas = THREAD_SUB_THREAD(thread,from_index);
 m_lg = 0.0; /* Initial Mass transfer rate*/
 if (Data_Valid_P())
  {
/* Identifies interface location*/
   if (C_VOF(cell,liq) != 0 && C_VOF(cell,liq) != 1)
    {
     if (C_T(cell,liq) > T_SAT)
     {
     m_lg = -0.127*C_VOF(cell,liq)*C_R(cell,liq)*
fabs(C_T(cell,liq)-T_SAT)/T_SAT; /* Evaporation*/
```

```
      }
     else if (C_T(cell,gas) < T_SAT)
      m_lg = 0.01*C_VOF(cell,gas)*C_R(cell,gas)*
fabs(T_SAT-C_T(cell,gas))/T_SAT; /* Condensation*/
     }
   }
 return (m_lg);
}
```

Appendix 3

METHANE DRY TEST SIMULATION DATA

In September 2015, experiments were carried out to obtain necessary data for the determination of the accommodation coefficients of liquid methane. In this section, the results of the dry tests that were run to characterise the thermal response of the 10-mm diameter Aluminum test cell is presented.

C.0.3 Domain and Boundary conditions

The domain for the methane dry tests is very similar to that of the hydrogen dry tests except for the addition of a stainless steel spacer between the sample-stick rod and the lid. The boundary and initial conditions remain unchanged as well. The meshed domain can be seen in Figure C.1. Here, the sensor in the helium space is named as D3, while the sensors S4,S3 and S2 in the hydrogen dry tests correspond to C2,D1 and D2 in the methane dry tests respectively.

C.0.4 Results

As with the hydrogen dry tests, the thermal model exhibits very good agreement with matching the transient thermal data of the sensors.

A plot of transient temperature profile for both the experimental and numerical curves for the sensors D3, C2,D1,and D2can be seen in Figures **??**,**??**,**??**, and **??**.A non-dimensionalised plot of the above figures can be seen in Figures **??**,**??**,**??**, and **??**. The dry test simulations for the methane test was facilitated though the use of advanced computational, storage, and networking infrastructure provided by the Hyak supercomputer system at the University of Washington.

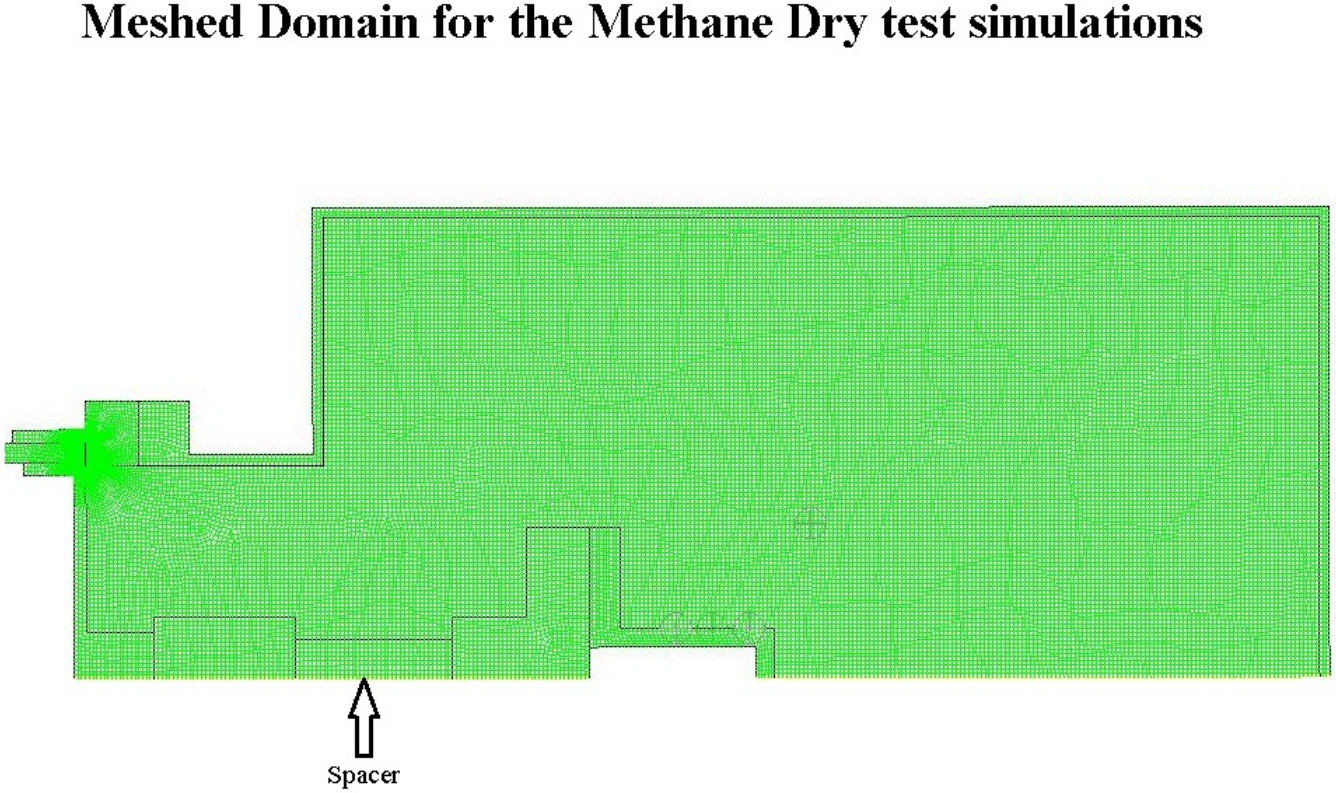

Figure C.1: Domain for the Dry test Simulation

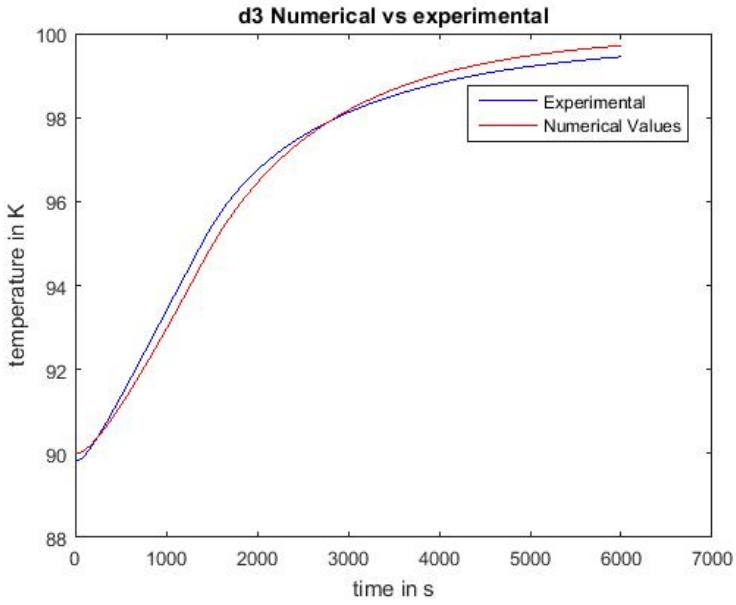

Figure C.2: Experimental and Numerical time response for the methane dry test cell experiment with the 10-mm diameter Aluminum test cell for Sensor D3

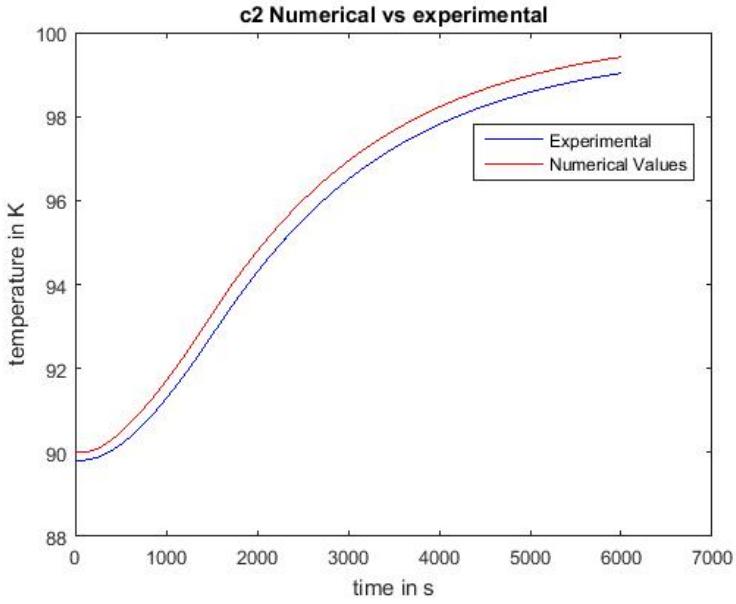

Figure C.3: Experimental and Numerical time response for the methane dry test cell experiment with the 10-mm diameter Aluminum test cell for Sensor C2

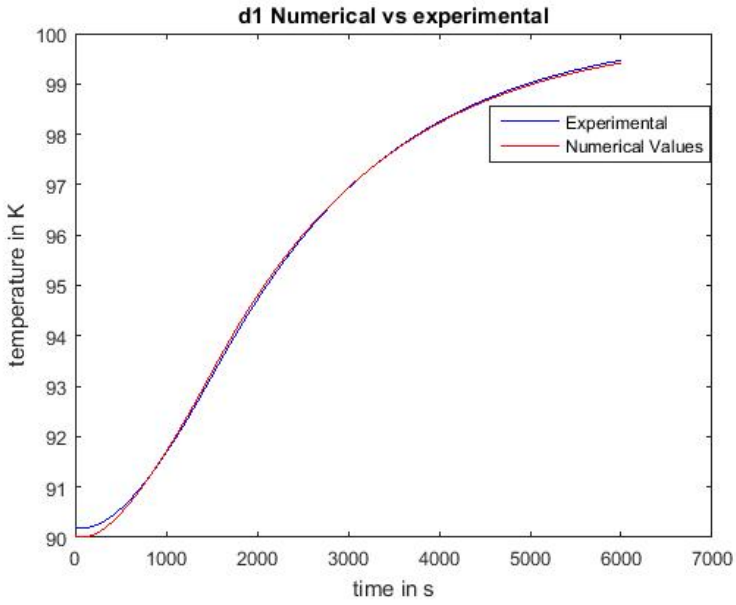

Figure C.4: Experimental and Numerical time response for the methane dry test cell experiment with the 10-mm diameter Aluminum test cell for Sensor D1

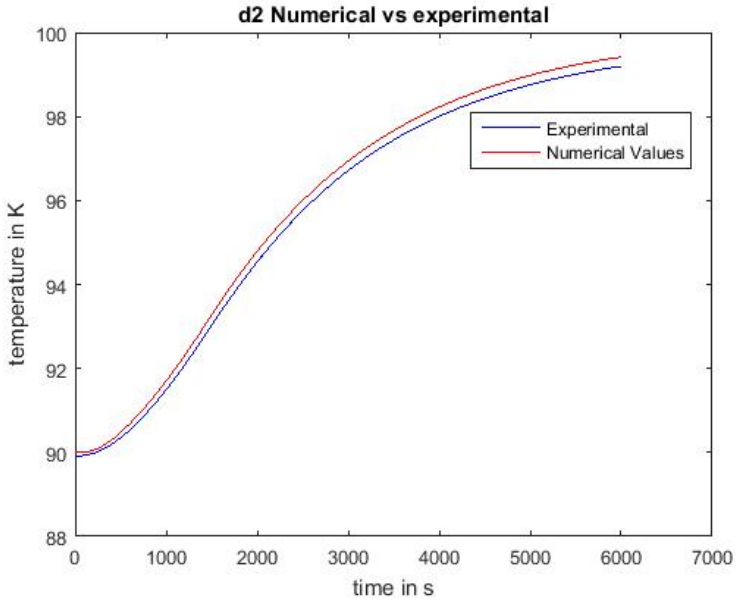

Figure C.5: Experimental and Numerical time response for the methane dry test cell experiment with the 10-mm diameter Aluminum test cell for Sensor D2

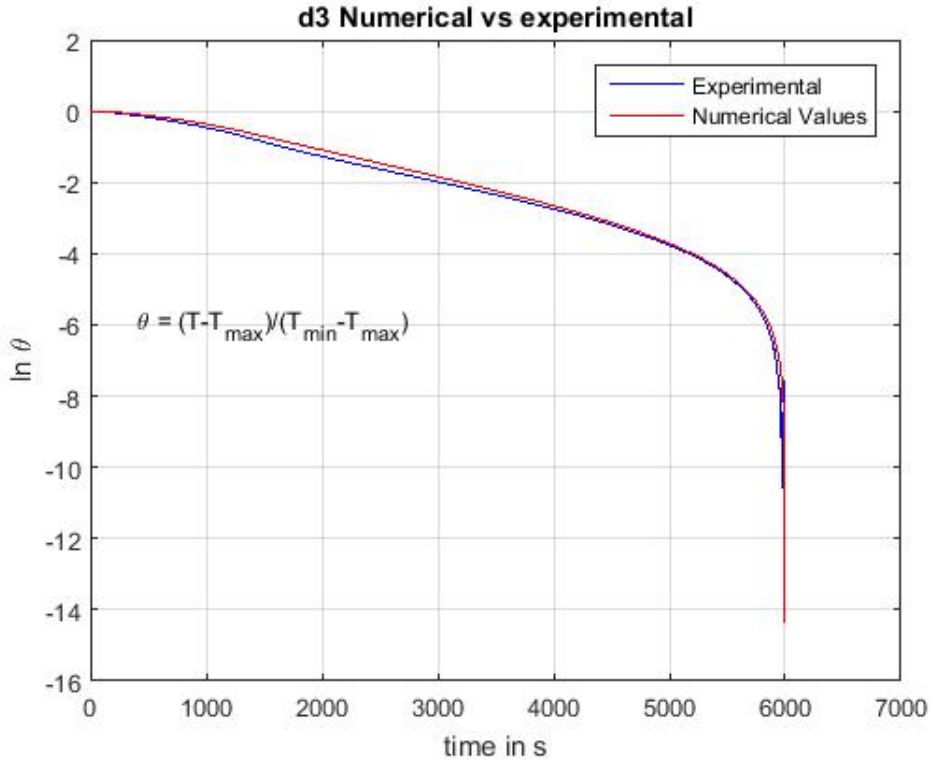

Figure C.6: Semi log plot of Experimental and Numerical time response for the dry test cell experiment with the 10-mm diameter Aluminum test cell for Sensor D3

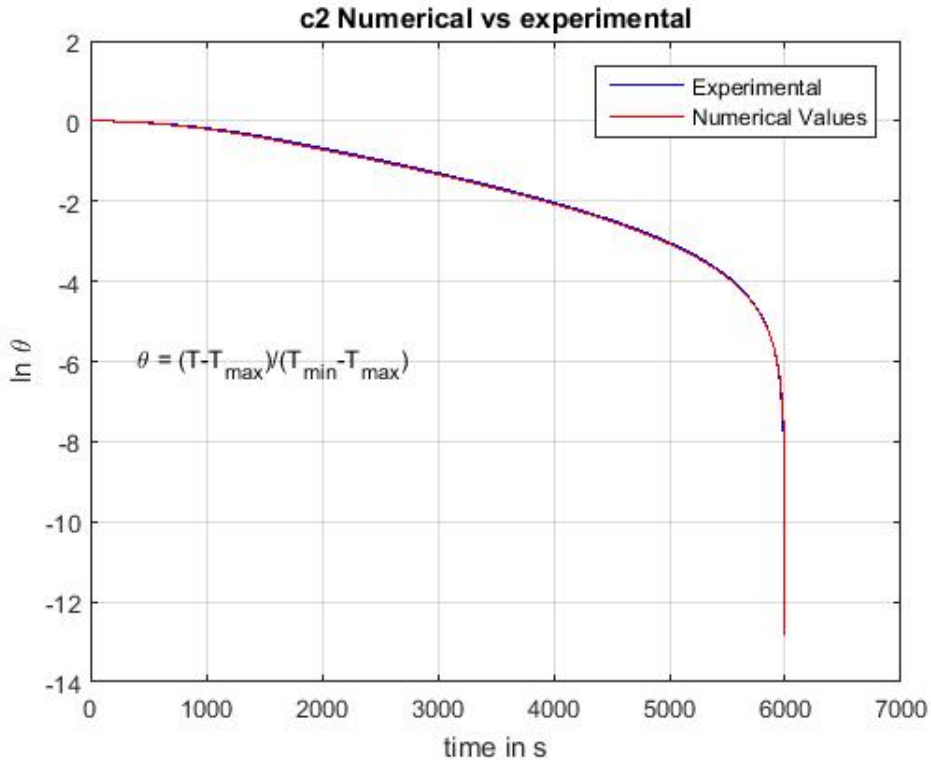

Figure C.7: Semi log plot of Experimental and Numerical time response for the dry test cell experiment with the 10-mm diameter Aluminum test cell for Sensor C2

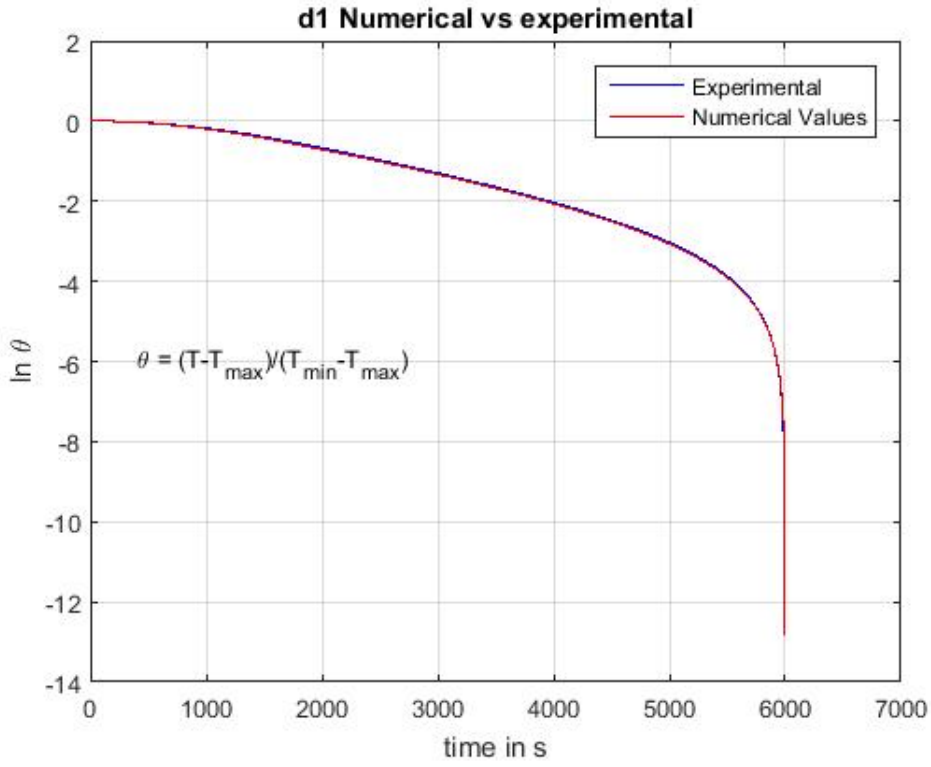

Figure C.8: Semi log plot of Experimental and Numerical time response for the dry test cell experiment with the 10-mm diameter Aluminum test cell for Sensor D1

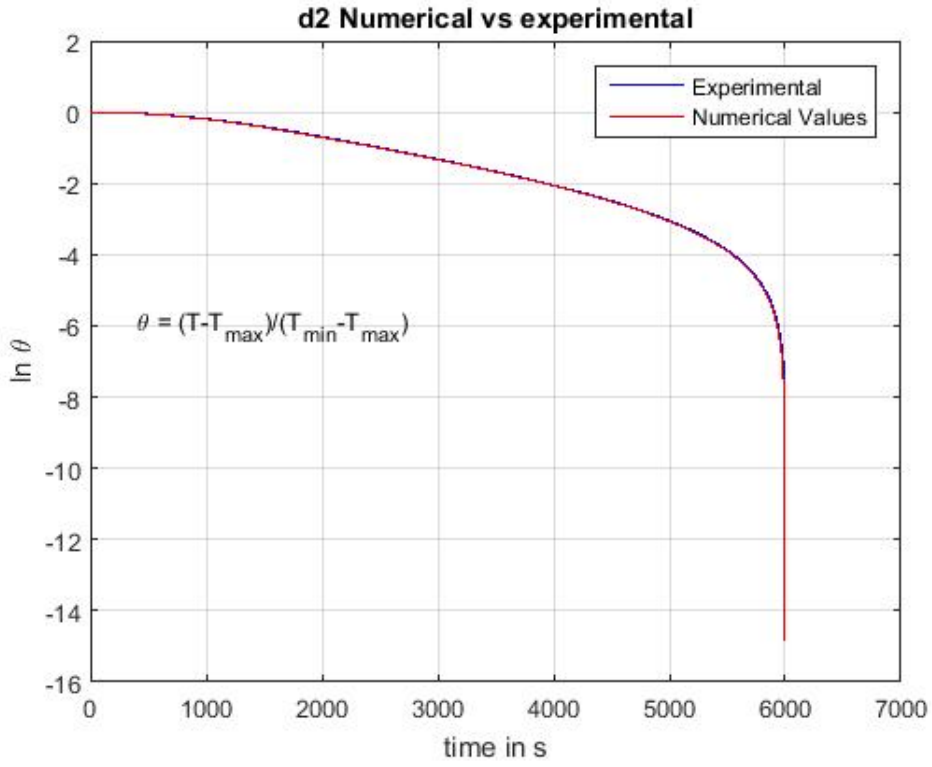

Figure C.9: Semi log plot of Experimental and Numerical time response for the dry test cell experiment with the 10-mm diameter Aluminum test cell for Sensor D2

Appendix 4

GRID ANALYSIS

Grid independence tests are essential in determining the precision of numerical simulations. The general procedures involves refining the grid, aka increasing the number of cells until the solution becomes grid independent. A comparison of the temperature time trace on one of the sensors (Sensor 3) is shown in Figure D.1. Based on the results, a grid size of 58k was chosen as the optimum match between the number of cells and computation resources required. As explained previously in the thesis, a plot of temperature time trace of the dry test simulation using a laminar model and the k-ϵ model is shown in Figure D.2. The dry test model with the k-ϵ model's enhanced wall treatment option was run with a significantly lower time step value than that of the laminar model, which helped in the reduction of computation time and resources. Also, a comparison of the effective turbulent viscosity with the plot of molecular viscosity along a line in the helium space showed that using the $k-\epsilon$ model did not damp or produce false viscosities. The value of turbulent viscosity turned out to be zero, which was expected for a laminar case.

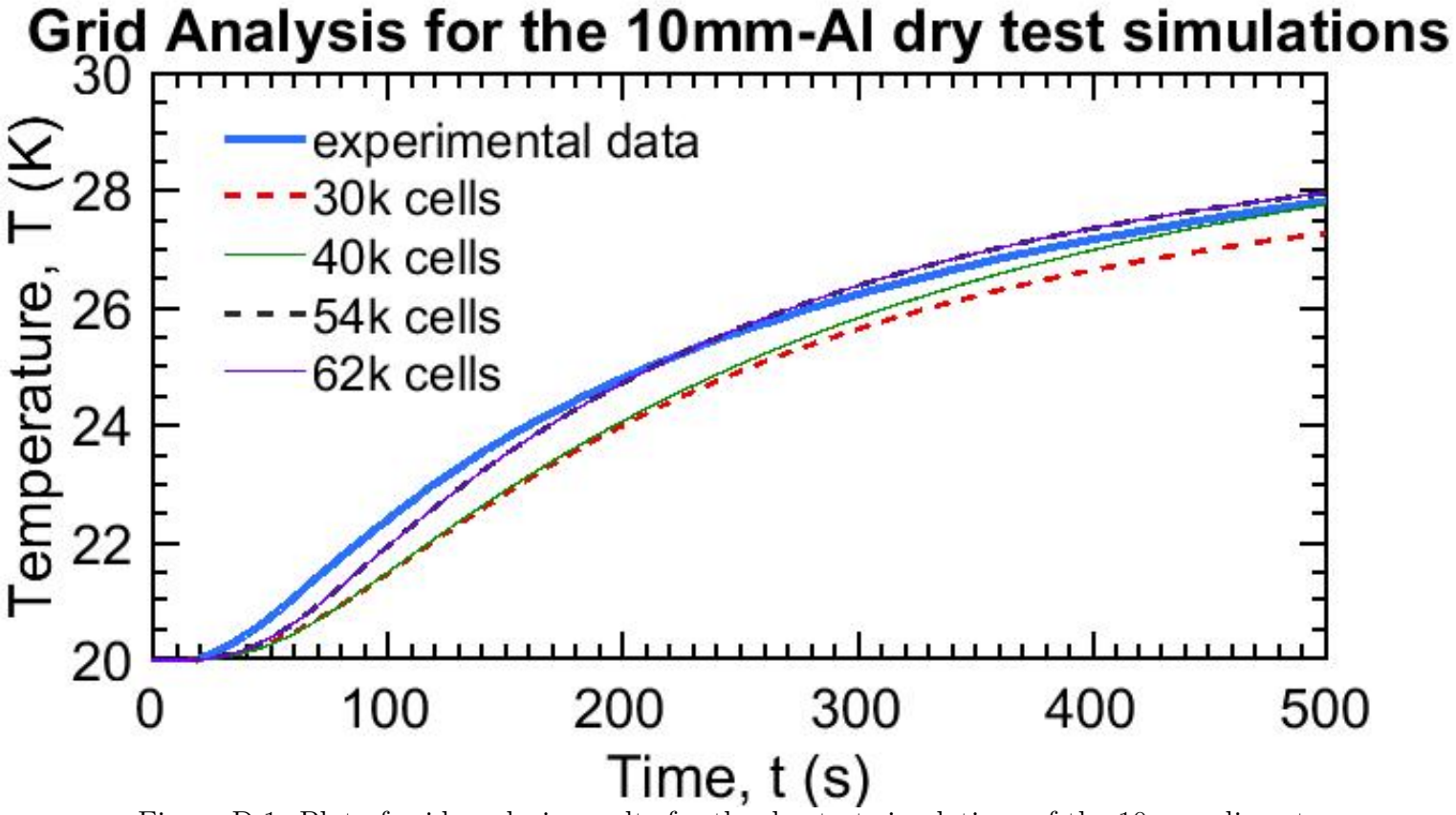

Figure D.1: Plot of grid analysis results for the dry test simulations of the 10-mm diameter Al test cell

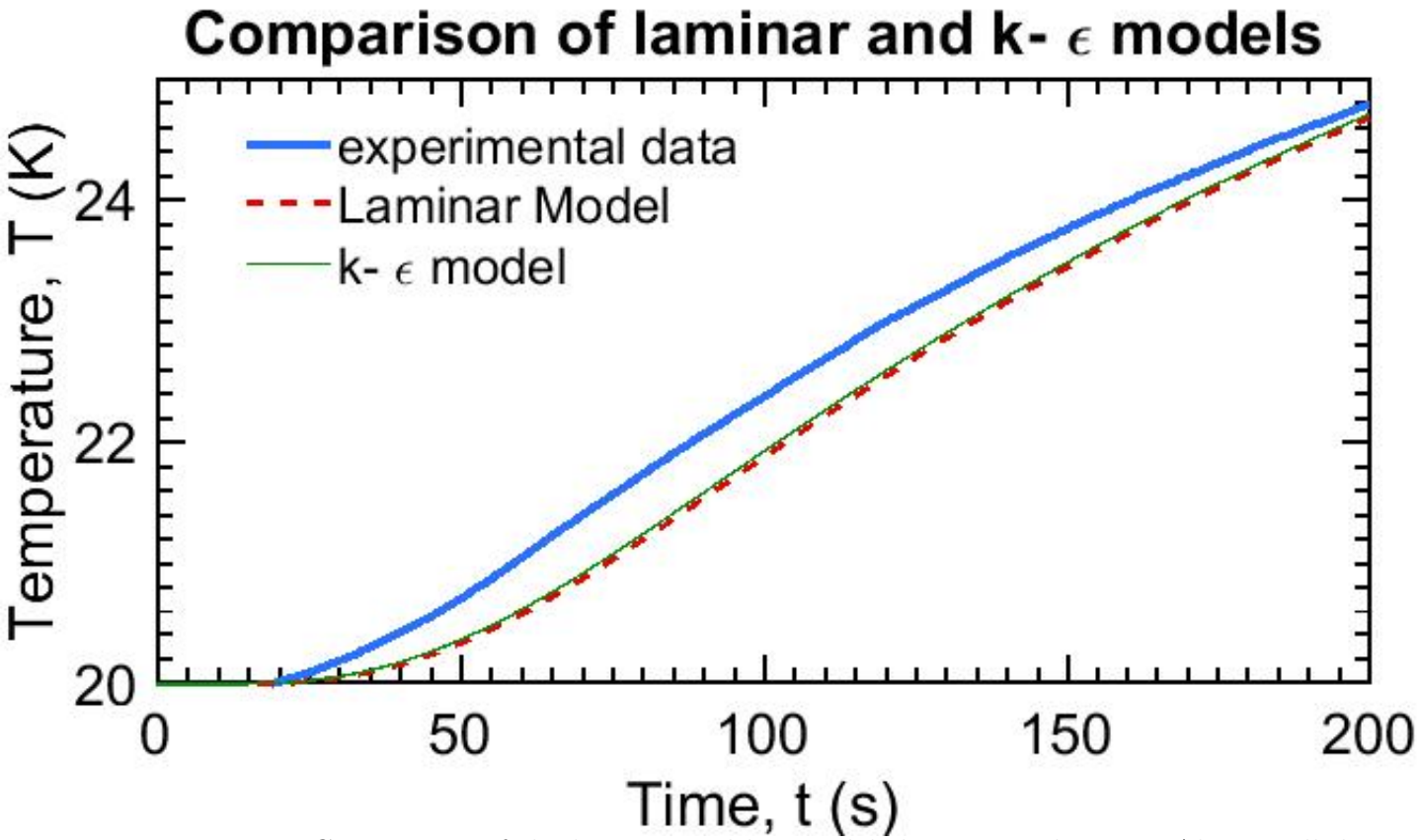

Figure D.2: Comparison of the laminar and k-ϵ model the 10-mm diameter Al test cell dry test simulations

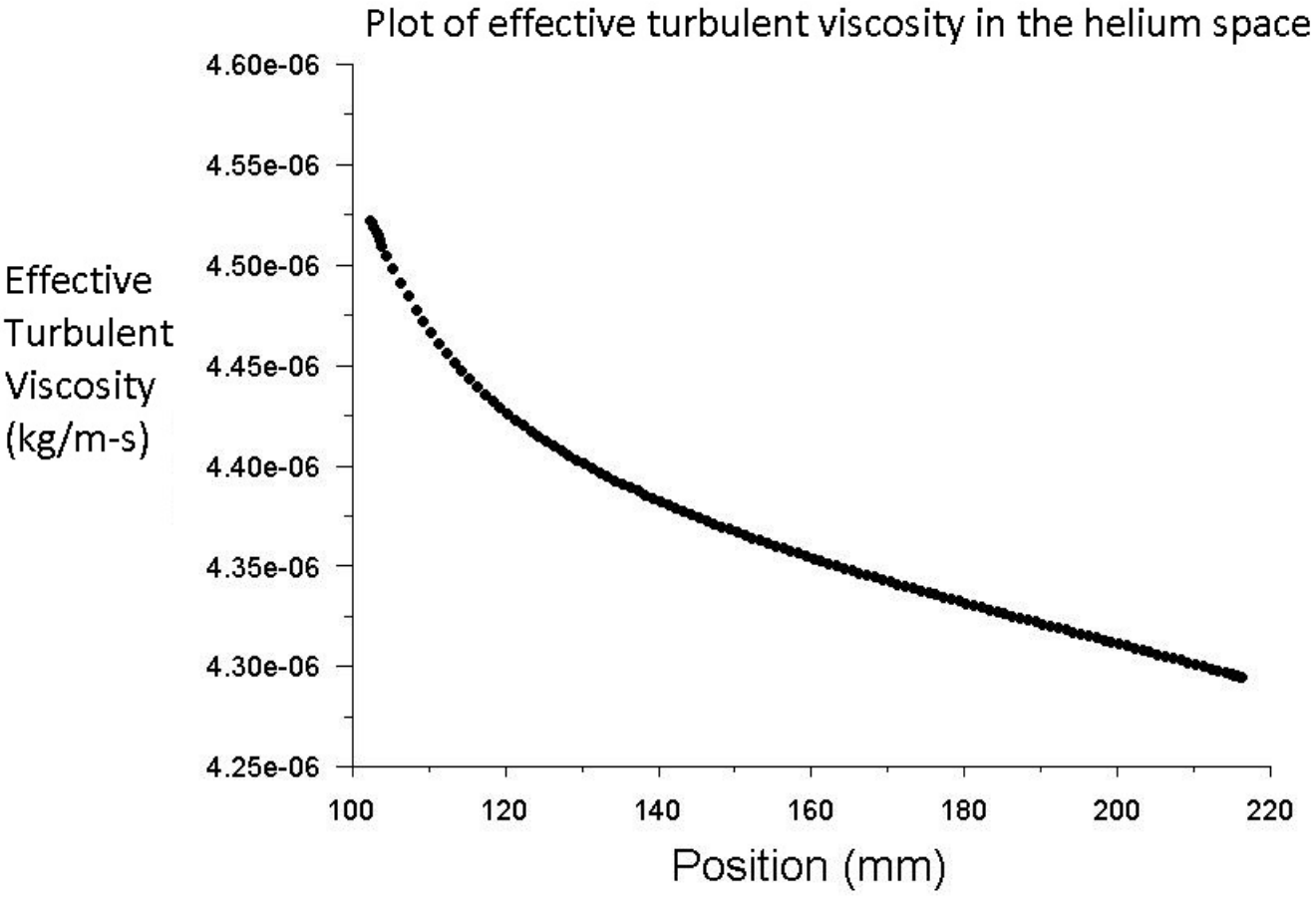

Figure D.3: Plot of effective turbulent viscosity in the helium space for the dry test simulation

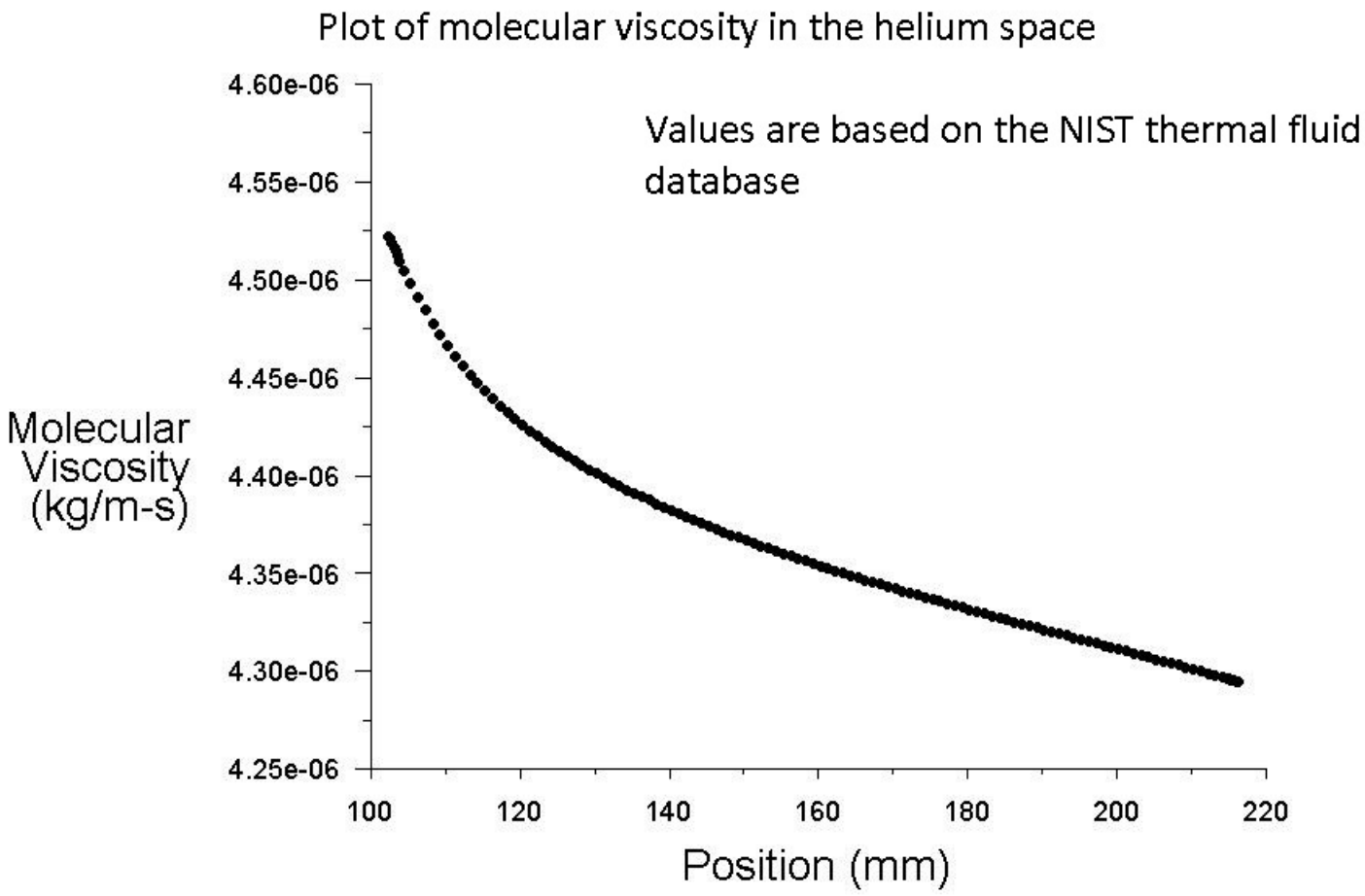

Figure D.4: Plot of molecular viscosity in the helium space for the dry test simulation

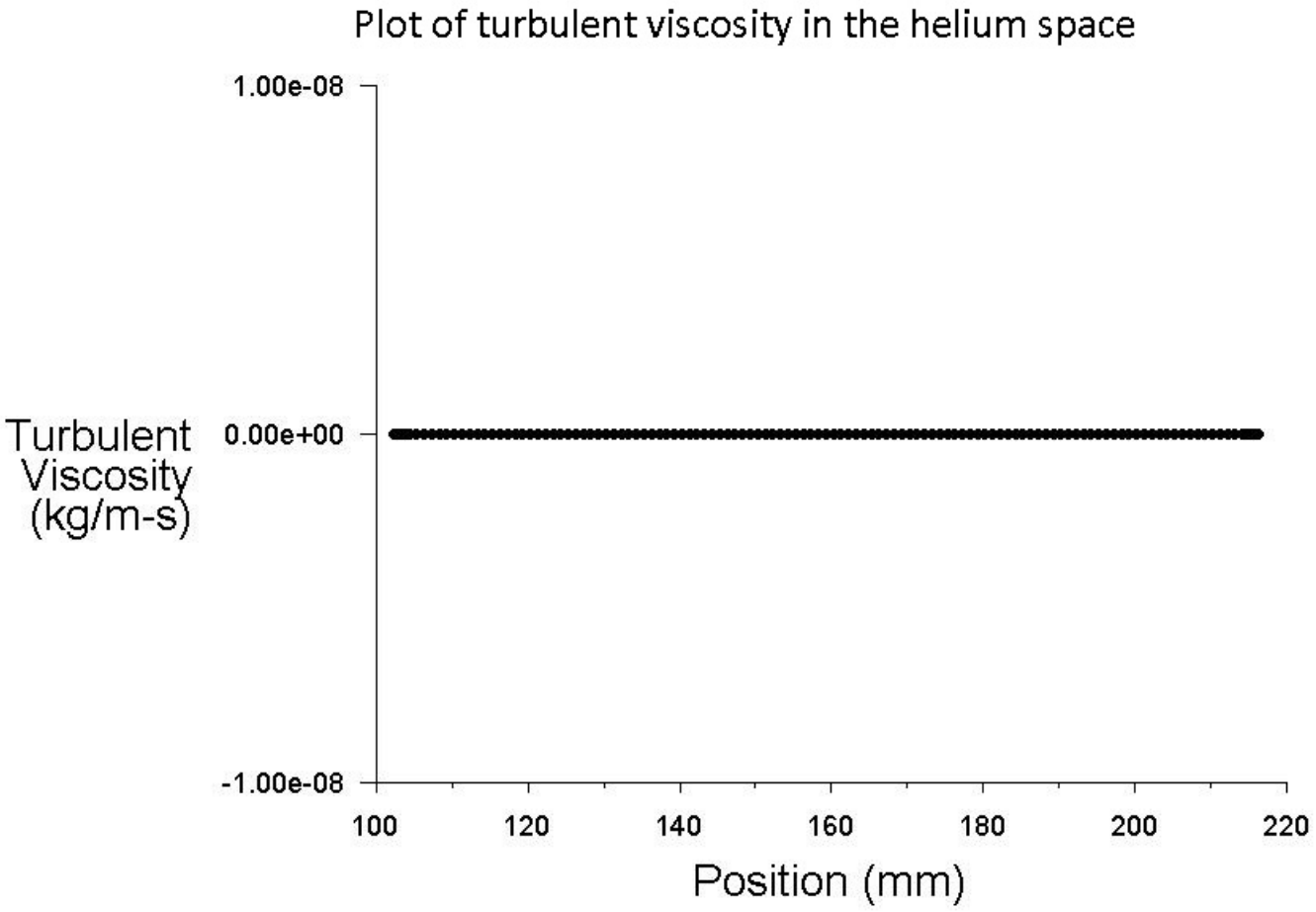

Figure D.5: Plot of turbulent viscosity in the helium space for the dry test simulation

BIBLIOGRAPHY

[1] SM Aceves, J Martinez-Frias, and O Garcia-Villazana. Analytical and experimental evaluation of insulated pressure vessels for cryogenic hydrogen storage. *International Journal of Hydrogen Energy*, 25(11):1075–1085, 2000.

[2] Vladimir S Ajaev. *Interfacial fluid mechanics*. Springer, 2012.

[3] Edouard Audi. Comparison of pressure-velocity coupling schemes for 2d flow problems. In *Advances in Computational Tools for Engineering Applications, 2009. ACTEA'09. International Conference on*, pages 245–248. IEEE, 2009.

[4] Jonathan Barrett and Charles Clement. Kinetic evaporation and condensation rates and their coefficients. *Journal of colloid and interface science*, 150(2):352–364, 1992.

[5] Kishan Bellur, Ezequiel Medici, Jeffrey Allen, Chang Kyoung Choi, Jimes Hermanson, Arun Tamilarasan, Daniel Hussey, David Jacobson, Juscelino B Leao, and John McQuillen. Neutron radiography of condensation and evaporation of hydrogen in a cryogenic condition. *Journal of Heat Transfer*, 137(8):080901, 2015.

[6] HK Cammenga, H Klinge, and B-E Rudolph. Untersuchungen über die verdampfungsgeschwindigkeit von flüssigkeiten. *Fortschrittsberichte über Kolloide und Polymere*, 55(1):118–123, 1971.

[7] BV Derjaguin and ZM Zorin. Optical study of the adsorption and surface condensation of vapours in the vicinity of saturation on a smooth surface. *Progress in Surface Science*, 40(1):83–117, 1992.

[8] Jeffrey R Feller, DW Plachta, G Mills, and C McLean. Demonstration of a cryogenic boil-off reduction system employing an actively cooled thermal radiation shield. 2008.

[9] ANSYS Fluent. Ansys fluent theory guide: Version 13.0. *Ansys Inc., Canonsburg*, 2010.

[10] David L Fritz III. Implementation of a phenomenological evaporation model into a porous network simulation for water management in low temperature fuel cells. 2012.

[11] Gustavo E C Fujiwara, Brock D Wiberg, B Woodard, and Michael B Bragg. 3d swept hybrid wing design method for icing wind tunnel tests. In *AIAA Paper 2104-2616, Atlanta, GA*, June 2014.

[12] Gustavo E C Fujiwara, Brian S Woodard, Brock D Wiberg, Andrew J Mortonson, and Michael B Bragg. A hybrid airfoil design method for icing wind tunnel tests. In *AIAA Paper 2013-2826, San Diego, CA*, June 2013.

[13] H Hertz. Ueber die verdunstung der flüssigkeiten, insbesondere des quecksilbers, im luftleeren raume. *Annalen der Physik*, 253(10):177–193, 1882.

[14] Cyril W Hirt and Billy D Nichols. Volume of fluid (vof) method for the dynamics of free boundaries. *Journal of computational physics*, 39(1):201–225, 1981.

[15] DS Hussey, DL Jacobson, M Arif, KJ Coakley, and DF Vecchia. In situ fuel cell water metrology at the nist neutron imaging facility. *Journal of Fuel Cell Science and Technology*, 7(2):021024, 2010.

[16] DS Hussey, DL Jacobson, M Arif, PR Huffman, RE Williams, and JC Cook. New neutron imaging facility at the nist. *Nuclear Instruments and Methods in Physics Research Section A: Accelerators, Spectrometers, Detectors and Associated Equipment*, 542(1):9–15, 2005.

[17] CP Karthikeyan and Anand A Samuel. Co 2-dispersion studies in an operation theatre under transient conditions. *Energy and Buildings*, 40(3):231–239, 2008.

[18] P Kittel, LJ Salerno, and DW Plachta. Cryocoolers for human and robotic missions to mars. In *Cryocoolers 10*, pages 815–821. Springer, 2002.

[19] M Knudsen. Maximum rate of vaporization of mercury. *Ann. Phys*, 47:697–705, 1915.

[20] M Knudsen. Maximum rate of vaporization of mercury. *Ann. Phys*, 47:697–705, 1915.

[21] Wen Ho Lee. A pressure iteration scheme for two-phase flow modeling. *Multiphase transport fundamentals, reactor safety, applications*, 1:407–431, 1980.

[22] Peter J Linstrom and William G Mallard. The nist chemistry webbook: A chemical data resource on the internet. *Journal of Chemical & Engineering Data*, 46(5):1059–1063, 2001.

[23] R Marek and J Straub. Analysis of the evaporation coefficient and the condensation coefficient of water. *International Journal of Heat and Mass Transfer*, 44(1):39–53, 2001.

[24] A Mehdizadeh, SA Sherif, and WE Lear. Numerical simulation of thermofluid characteristics of two-phase slug flow in microchannels. *International Journal of Heat and Mass Transfer*, 54(15):3457–3465, 2011.

[25] Sashidhar S Panchamgam, Arya Chatterjee, Joel L Plawsky, and Peter C Wayner. Comprehensive experimental and theoretical study of fluid flow and heat transfer in a microscopic evaporating meniscus in a miniature heat exchanger. *International Journal of Heat and Mass Transfer*, 51(21):5368–5379, 2008.

[26] Charles Panzarella, David Plachta, and Mohammad Kassemi. Pressure control of large cryogenic tanks in microgravity. *Cryogenics*, 44(6):475–483, 2004.

[27] David Plachta and Peter Kittel. An updated zero boil-off cryogenic propellant storage analysis applied to upper stages or depots in an leo environment. *AIAA Paper*, 3589:7–10, 2002.

[28] P Kittel'andD W Plachta. Propellant preservation for mars missions. *Advances in Cryogenic Engineering Volume 45 (Parts A & B)*, 45:443, 2000.

[29] Joel L Plawsky, Manas Ojha, Arya Chatterjee, and Peter C Wayner Jr. Review of the effects of surface topography, surface chemistry, and fluid physics on evaporation at the contact line. *Chemical Engineering Communications*, 196(5):658–696, 2008.

[30] G Preiss and PC Wayner. Evaporation from a capillary tube. *Journal of Heat Transfer*, 98(2):178–181, 1976.

[31] William J Rider and Douglas B Kothe. Reconstructing volume tracking. *Journal of computational physics*, 141(2):112–152, 1998.

[32] Adam Robinson, Hervé Morvan, and Carol Eastwick. Computational investigations into draining in an axisymmetric vessel. *Journal of Fluids Engineering*, 132(12):121104, 2010.

[33] M Isabel Roldán, Loreto Valenzuela, and Eduardo Zarza. Thermal analysis of solar receiver pipes with superheated steam. *Applied Energy*, 103:73–84, 2013.

[34] SC Rybak, GS Willen, WH Follett, GJ Hanna, EC Cady, E DiStefano, and JS Meserole. Feasibility study for a cryogenic on-orbit liquid depot-storage, acquisition and transfer (cold-sat) satellite. *Final Report, Feb. 1988-Mar. 1990 Ball Aerospace Systems Div., Boulder, CO.*, 1, 1990.

[35] Dong-Liang Sun, Jin-Liang Xu, and Li Wang. Development of a vapor–liquid phase change model for volume-of-fluid method in fluent. *International Communications in Heat and Mass Transfer*, 39(8):1101–1106, 2012.

[36] S Vodret, D Vitale Di Maio, and G Caruso. Numerical simulation of turbulent forced convection in liquid metals. In *Journal of Physics: Conference Series*, volume 547, page 012033. IOP Publishing, 2014.

[37] Peter C Wayner. The effect of interfacial mass transport on flow in thin liquid films. *Colloids and Surfaces*, 52:71–84, 1991.

[38] Sang-Kwon Wee, Kenneth D Kihm, David M Pratt, and Jeffrey S Allen. Microscale heat and mass transport of evaporating thin film of binary mixture. *Journal of thermophysics and heat transfer*, 20(2):320–326, 2006.

[39] Qingfang Wu and Harris Wong. A slope-dependent disjoining pressure for non-zero contact angles. *Journal of Fluid Mechanics*, 506:157–185, 2004.